Biomaterials Advances 182 (2026) 214723

Contents lists available at ScienceDirect

Biomaterials Advances

journal homepage: www.journals.elsevier.com/materials-science-and-engineering-c

Sulfated poly(aspartic acid) coatings as next-generation biomimetic interfaces for blood-contacting devices

Cuong Hung Luu [a], Akriti Nepal [a], Nam-Trung Nguyen [b,c], Hang Thu Ta [a,b,*]

[a] School of Environment and Science, Griffith University, Nathan, QLD, 4111, Australia
[b] Queensland Quantum and Advanced Technologies Research Institute, Griffith University, Nathan, QLD, 4111, Australia
[c] School of Engineering and Built Environment, Griffith University, Nathan, QLD, 4111, Australia

ARTICLE INFO

Keywords:
Poly(aspartic acid)
Sulfated
Biomimetic surface coating
Antithrombogenic
Antibacterial

ABSTRACT

The increasing reliance on blood-contacting medical devices underscores the need for materials that minimise thrombosis and inflammation. Devices such as stents and dialysis membranes often face complications related to clot formation and microbial colonisation. To address these challenges, this study explored the development of sulfated poly(aspartic acid) (sPASP) coatings aimed at improving haemocompatibility and reducing infection risk. PASP, a biodegradable, biocompatible polymer, and calcium chelator, served as the base material, with sulfation introduced to enhance its antithrombotic, antibacterial, and anti-inflammatory properties. Sulfate groups mimic natural anticoagulants such as heparin, potentially promoting antithrombin activity and inhibiting clot development. The coatings were fabricated *via* a simplified one-pot process on polydopamine-modified substrates. The degree of sulfation was systematically varied from 10% to 80% to optimise the material's performance and thoroughly evaluated across multiple dimensions of blood compatibility. Assessments included surface physicochemical properties, protein adsorption, platelet adhesion, antithrombotic efficacy, cellular compatibility, and antibacterial activity, under static and dynamic conditions. Notably, sPASP with a sulfation degree of 40% exhibited the most favourable blood compatibility, demonstrating strong potential compared to heparin-mimicking polysaccharide coatings. In addition, the material exhibited excellent *in vivo* biocompatibility in implantation models, further underscoring its promise as a high-performance, multifunctional biomimetic interface for blood-contacting biomedical applications.

1. Introduction

Blood-contacting medical devices play a critical role in modern healthcare, encompassing a diverse array of applications including intravascular stents, prosthetic heart valves, dialysis membranes, and extracorporeal membrane oxygenation systems [1,2]. These devices are designed to interface directly with blood, a complex biological fluid inherently predisposed to initiate coagulation upon contact with foreign surfaces [3]. Consequently, there is an urgent need to engineer materials and surfaces to be more haemocompatible and capable of interacting with blood without provoking adverse events such as thrombosis, haemolysis, or immune activation [4]. Compounding this challenge is the risk of bacterial colonisation, which can lead to persistent infections and device failure [5,6]. Therefore, the design of such devices demands a nuanced approach, ensuring therapeutic efficacy while mitigating thrombotic and microbial complications [1].

A variety of strategies have been employed to address thrombogenicity and infection risk. Among these, surface modifications incorporating antithrombotic and antimicrobial functionalities have received considerable attention [3]. Heparin-based coatings, for example, have been widely adopted due to their ability to inhibit the coagulation cascade [7]. Concurrently, antimicrobial strategies, such as the inclusion of silver nanoparticles or antibiotic-laden materials, have been explored to suppress microbial adhesion and biofilm formation [8–10]. Beyond such approaches, the rational design of novel biomaterials with intrinsic antithrombotic and antibacterial properties has also gained momentum [11]. These materials typically exhibit high biocompatibility and controlled degradation profiles, essential for long-term implant safety [12–14]. Other innovative solutions include drug-eluting surfaces for localised delivery of therapeutic agents, and biomimetic designs that

* Corresponding author at: School of Environment and Science, and Queensland Quantum and Advanced Technologies Research Institute, Griffith University, Nathan Campus, Brisbane, QLD, 4111, Australia.
E-mail address: h.ta@griffith.edu.au (H.T. Ta).

https://doi.org/10.1016/j.bioadv.2026.214723
Received 31 August 2025; Received in revised form 28 December 2025; Accepted 17 January 2026
Available online 19 January 2026
2772-9508/© 2026 The Authors. Published by Elsevier B.V. This is an open access article under the CC BY license (http://creativecommons.org/licenses/by/4.0/).

replicate the non-thrombogenic and anti-adhesive characteristics of native vascular structures [1,15,16]. Together, these approaches reflect an advanced understanding of host–material interactions and guide the next generation of safer and more functional blood-contacting devices.

Among the promising candidates in this field, sulfated polysaccharides have garnered particular interest due to their dual bioactivity [17]. Although heparin-based coatings have long been considered the gold standard for enhancing blood compatibility, their extraction from animal sources presents challenges, including batch-to-batch variability and stability issues [18–20]. The application of sulfated polymers in surface coatings for antithrombotic purposes remains largely underexplored [21]. One of the few studies in this area by Neto et al. employed sulfated chitosan; however, the material exhibited only limited inhibition of platelet adhesion, and the broader effects on blood compatibility, both *in vitro* and *in vivo*, were inadequately addressed [18]. Similarly, the work of Ma et al. did not demonstrate outstanding antithrombotic performance, and the study lacked evaluations of blood–material interactions under physiological shear stress as well as *in vivo* assessments [19]. In light of these limitations, the present study proposes the use of a novel material distinct from conventional polysaccharides: a poly(amino acid)-based polymer that has been chemically sulfated to emulate the anticoagulant activity of heparan sulfate. Owing to its semi-synthetic origin derived from amino acids, the sulfated variant is anticipated to retain the capacity to catalyse the activation of antithrombin III (ATIII), thereby affording a more effective antithrombotic mechanism when compared with conventional polymer brushes based on highly charged or zwitterionic polymers [21–24]. Furthermore, conventional surface coating methods involving synthetic polymers often necessitate multiple complex steps to achieve effective grafting. In contrast, a one-pot reaction has emerged as an optimal and efficient alternative [2]. Notably, most previous studies have primarily assessed materials *in vitro* using tissue culture plates, which fail to accurately replicate the dynamic interactions with blood flow [1,25]. Building upon these identified research gaps, the rationale for the present study was gradually developed to ensure its relevance and applicability to real-world biomedical conditions.

In literature, poly(aspartic acid) (PASP), well known as a biodegradable and biocompatible polymer, is receiving increasing attention in the biomedical field for its potential applications. The intrinsic properties of PASP, such as its natural biodegradability and non-toxicity, make

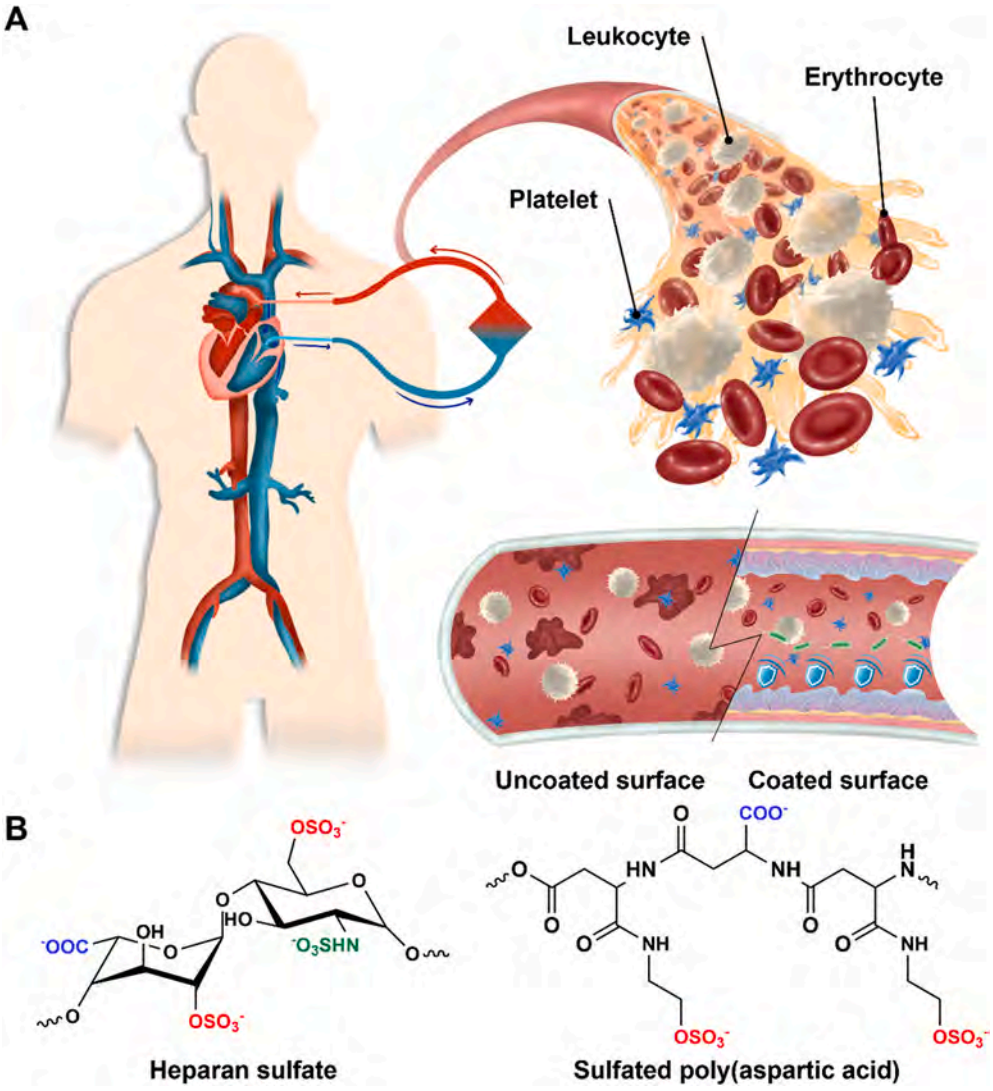

Scheme 1. Illustration of potential outcomes for blood-contacting medical devices when applied in the human body. (A) These devices may directly interact with fundamental blood components such as leukocytes, erythrocytes, and platelets, subsequently triggering primary responses including surface-induced coagulation and the risk of infection owing to bacterial colonisation on the device surface. Nevertheless, such adverse effects could be mitigated through surface coating strategies employing antimicrobial and antithrombotic materials. (B) Schematic representation of the similarity in molecular structures of heparan sulfate (heparin) and sulfated poly(aspartic acid) (sPASP), proposed for application in surface coatings to enhance anticoagulant and antibacterial performance.

it a compelling alternative to traditional polymers used in medical applications [26–29]. Furthermore, PASP effectively chelated calcium. This characteristic accounted for its anticoagulant potential, as calcium is essential to the clotting process [26,28,29]. Chelators such as citrate bind to calcium ions, preventing them from participating in coagulation, thereby effectively reducing the blood's tendency to clot [30,31]. This motivates us to employ PASP for surface coating. Based on the aforementioned objectives concerning antithrombotic and antibacterial coatings, we proposed the use of PASP as a poly(amino acid)-based backbone, subsequently modifying the material with sulfate groups to mimick heparin-like activity in promoting antibacterial and antithrombotic functions [21]. Sulfated PASP (sPASP) was anticipated to combine the inherent biocompatibility of its base component, the non-essential amino acid L-aspartic acid, with its calcium chelation capability, and anticoagulant activity comparable to heparin. Beyond reducing the risk of device-related infections and thrombus formation, sPASP was also expected to mitigate localised inflammation and limit the production of reactive oxygen species (ROS) by leukocytes upon contact with medical devices. This hypothesises multifunctionality and positions sPASP as a highly promising material for biomedical coatings, capable of addressing the challenges associated with blood-contacting devices through the use of amino acid-derived polymer as a potential alternative to natural heparin (See Scheme 1).

In summary, we hypothesised that sPASP would enhance anticoagulant performance at the material–blood interface. To test this, we fabricated surface coatings using PASP as the base polymer, modified *via* a one-pot sulfation reaction, and applied them to PET membranes as representative medical device substrates. The degree of sulfation was systematically varied to assess its impact on anticoagulant and antibacterial properties. Surface characterisation was conducted using ATR-FTIR, XPS, AFM, ellipsometry, and surface energy measurements. Biocompatibility was evaluated through haemolysis and cytocompatibility tests with endothelial cells and macrophages, both key in blood-contact scenarios. Anticoagulant efficacy was assessed *via* non-specific protein adsorption, platelet adhesion, and coagulation time assays. To simulate physiological conditions, we also performed dynamic testing using a microfluidic device and Chandler loop. Surface stability and bacterial anti-adhesion of the coatings were also examined for biomedical relevance. Finally, *in vivo* subcutaneous implantation in mice was conducted to evaluate host response and material safety. Overall, the study developed a promising alternative to natural glycosaminoglycans, demonstrating effective anticoagulant and antimicrobial surface properties, supporting sPASP's potential as a biomimetic coating for blood-contacting medical devices.

2. Materials and methods

2.1. Materials

L-aspartic acid (≥ 98%), sulfolane (99%), phosphoric acid (≥ 85 wt% in H_2O), dopamine hydrochloride (≥ 98%), 2-aminoethyl hydrogen sulfate (≥ 98%), and 1-ethyl-3-(3-dimethylaminopropyl) carbodiimide (EDC, ≥ 99%) were procured from Sigma-Aldrich, Inc. (MO, USA). Other common reagents were sourced from either Sigma-Aldrich, Inc. (MO, USA) or Thermo Fisher Scientific Inc. (MA, USA). All chemicals were purchased and used directly without undergoing any further purification. The substrates employed in this study were fabricated from pure polyethylene terephthalate (PET) and sourced from a local supplier. The PET sheet was sectioned into circular substrates with a diameter of 6 mm and an approximate thickness of 1 mm to facilitate evaluations under *in vitro* and *in vivo* conditions.

2.2. Synthesis of PSI

In this experiment, the synthesis of polysuccinimide (PSI) commenced with the preparation of materials and equipment. An oil bath was preheated to 185 °C for 1 h, and an overhead stirring system was assembled. Nitrogen gas was supplied to the system and verified *via* displacement in a water beaker. For the reaction, 14 g of *L*-aspartic acid and 56 g of sulfolane were placed into a 100 mL round-bottom flask. Subsequently, 1 mL of phosphoric acid, collected using the preheated pipette tip, was added to the reaction mixture. The suspension was subjected to continuous mechanical stirring at 250 rpm within the preheated oil bath under a nitrogen atmosphere. After 5 h of reaction, the resultant product was precipitated into a large volume of deionised water (DIW), washed repeatedly with the same, and harvested by centrifugation at 5000 ×*g*. The final pellet was dried in a vacuum oven for four days and subsequently stored under ambient conditions.

2.3. Synthesis of PASP

To transform PSI into PASP, 50 mg of sodium hydroxide (1.25 mmol) was combined with 100 mg of PSI powder (succinimide molecular weight 97.07 $g{\cdot}mol^{-1}$, 1.03 mmol) in a 5 mL water solution and left to incubate at room temperature for 2 h. It is important to note that an additional amount of sodium hydroxide, approximately 1.2 times the molar amount of succinimide units, was utilised to guarantee thorough hydrolysis. The resultant sodium polyaspartate was then isolated by precipitation in methanol and underwent multiple washes to eliminate any remaining NaOH. Finally, the precipitate was subjected to freeze-drying.

2.4. Preparation of sPASP coatings

In our study, PET surfaces (both sides) were modified using polydopamine (PDA) and further coated with sulfated poly(aspartic acid). Initially, the PET substrates were cleansed using a 30% (v/v) ethanol under ultrasonication for 10 min. The cleaned substrates were then immersed in a dopamine solution (2 $mg{\cdot}mL^{-1}$, Tris buffered saline, pH 8.5) for 2 h at room temperature to facilitate PDA deposition on PET membrane, producing what we briefly termed PDA. The PDA-coated surfaces were subsequently immersed in a PASP solution at a concentration of 2 $mg{\cdot}mL^{-1}$. To modulate the degree of sulfation, 2-aminoethyl hydrogen sulfate (AHS) was introduced at varying molar ratios ranging from 0% to 80% relative to the molar amount of succinimide units in the PASP solution. To facilitate the coupling reaction, EDC was employed as a carboxyl group activator to facilitate the conjugation of AHS and PASP. The heparinised sample (HEP) used for comparison with the optimal sPASP formulation was prepared using the same reaction conditions. Specifically, AHS was omitted from the process, and heparin ammonium salt from porcine intestinal mucosa (Sigma-Aldrich, Inc., MO, USA) was used instead of PASP. The molar ratio of EDC for the aforementioned reaction was detailed in Table S1. The one-pot reaction for coating both sides of the substrate was carried out overnight at ambient temperature, with continuous stirring at 500 rpm. The resultant surfaces with different substitution percentages of sulfate moieties were shortly designated as PASP, sPASP10, sPASP20, sPASP40, sPASP 60, sPASP80. The final product was washed three times with DIW and stored at 4 °C for further experimental use.

2.5. Surface characterisation of sPASP coatings

2.5.1. Functionalities density

A comprehensive analysis of the surface chemical compositions of various coatings on PET substrates was conducted. The quantification of amine groups on surfaces was conducted through an AO II colorimetric staining technique. The process involved adjusting the pH of the AO II solution to 4 using hydrochloric acid buffer, followed by immersing the samples in this solution for a duration of 2 h. The samples were then cleansed with hydrochloric acid at the same pH value and the AO II that had bound to the surface was subsequently released using a sodium hydroxide solution with a pH of 11. The solution containing the

desorbed AO II was then subjected to absorbance measurement at a wavelength of 485 nm utilising a microplate reader (CLARIOstar® Plus, BMG LABTECH GmbH, Germany). The amine group concentration was determined from these absorbance values, referencing a pre-established standard curve. Similar techniques were employed to quantify carboxyl and sulfate groups using TBO colorimetric method. *Vice versa*, the assay underwent the adsorption of free TBO molecules at pH 11 and the desorption of attached TBO molecules at pH 4, followed by reading absorbance at 650 nm.

2.5.2. Surface energy

Water contact angle (WCA) measurements for the sPASP coatings were performed at ambient temperature using the contact angle system (Attension® Theta Flex, Biolin Scientific AB, Sweden). This analysis was carried out using the sessile drop of 5 μL of deionised water, diiodomethane (DIM), and dimethylformamide (DMF), with images captured and analysed through the OneAttension software. For each sample, a minimum of 3 distinct readings were recorded to determine the WCA. Surface energy (SFE) of each sample was applied to the Fowkes theory to calculate the polar (γ^p) and dispersive (γ^d) components of the surface energy. Additionally, the liquid surface tension and solid surface tension were abbreviated as γ_L and γ_S, respectively [32].

$$\gamma_L(1+cos\theta) = 2\sqrt{\gamma_L^p \bullet \gamma_S^p} + 2\sqrt{\gamma_L^d \bullet \gamma_S^d} \quad (1)$$

2.5.3. Elemental analysis

The elemental analysis of the coatings was done using X-ray photoelectron spectroscopy (XPS, XSAM200, Kratos Analytical Ltd., UK), equipped with a monochromatic Al Kα source (1486.6 eV) and operating at 12 kV × 15 mA under a vacuum of 20×10^{-6} Pa. Comprehensive XPS scans were conducted ranging from 0 to 1200 eV using a 300-eV pass energy, at increments of 0.5 eV. High-resolution scans were also obtained for specific peaks of interest, using a step size of 0.05 eV and totaling 15 min of acquisition time per sample. The chemical properties of the coatings were analysed using attenuated total reflectance Fourier transform infrared spectra (ATR-FTIR, Spectrum Two FTIR Spectrometer, PerkinElmer Inc., USA). A ^{1}H NMR spectrophotometer (Avance III HD 500 MHz, Bruker Corporation, Germany) was also employed to analyse the chemical structures of PSI and PASP following synthesis.

2.5.4. Surface characteristics

The thickness of the polymeric coatings on the PET films was determined using filmetric reflectometer (Filmetrics F54, KLA Corporation, USA). The surface morphology of these substrates was meticulously observed through scanning electron microscopy (SEM, JSM-6510LV, JEOL Ltd., Japan) and atomic force microscopy (AFM, Park NX10, Park Systems Corp., South Korea).

2.6. Sterilisation of sPASP coatings

To prepare samples for both *in vitro* and *in vivo* studies, a sterilisation process was performed using 70% (v/v) alcohol. Following sterilisation, the surfaces were allowed to dry in a sterile environment. Subsequently, the samples were either immersed in phosphate-buffered saline (PBS, pH 7.4) for 2 h and used immediately, or they were rinsed with pure water and air-dried for storage.

2.7. Protein adsorption on sPASP coatings

The efficacy of sPASP coatings in resisting protein adsorption was assessed using bovine serum albumin (BSA), fibrinogen (FBG), and platelet-poor plasma (PPP) as representative proteins. The experimental procedure involved initially immersing substrates in PBS at 37 °C for 1 h. This was followed by their incubation in individual protein solutions (5 mg·mL^{-1} BSA, 1 mg·mL^{-1} FBG, and 10% PPP) at the same temperature for 2 h. The concentrations of BSA and FBG were applied by the approximate concentration of these proteins in human plasma, while 10% PPP can show the general effect of plasma protein binding [3,33]. Post incubation, the samples were thoroughly rinsed thrice with PBS and then subjected to a 2 wt% sodium dodecyl sulfate (SDS) solution, and sonicated for 30 min to release any adsorbed proteins. The extent of protein adsorption on each sample was quantitatively analysed using the bicinchoninic acid reagent (Micro BCA™ Protein Assay Kit, Thermo Fisher Scientific Inc., MA, USA), according to the manufacturer's instructions. Absorbance readings were taken at 562 nm using a microplate reader, with the process being repeated for three independent trials to ensure statistical relevance.

2.8. Haemolytic activity of sPASP coatings

Red blood cells (RBCs) was employed to assess the haemocompatibility of PASP solutions and sPASP surface coatings. Whole blood (obtained from Australian Red Cross Blood Service) was centrifuged at 1000 ×*g* for 15 min. Subsequently, the supernatant plasma layer was removed, and the RBCs were collected and diluted 1:50 with PBS. For PASP solutions, 20 μL of each sample was incubated with 180 μL of the RBC solution at 37 °C and under shaking at 200 rpm for 24 h. For sPASP surface coatings, the incubation involved 400 μL of the RBC solution with the coated surfaces for the same durations. In both cases, 1% Triton X-100 and PBS were utilised as positive and negative controls. Post-incubation, the mixtures were centrifuged at 1000 ×*g* for 15 min to facilitate separation of intact RBCs from the supernatant. Photographic documentation of the supernatant was conducted, followed by the measurement of optical density (OD) at 545 nm to quantify haemoglobin release. The percentage of haemolysis was calculated using equation below [34].

$$Haemolysis\ (\%) = \frac{OD_{sample} - OD_{negative}}{OD_{positive} - OD_{negative}} \times 100\% \quad (2)$$

2.9. Cytocompatibility of sPASP coatings

2.9.1. Cell culture

Mouse endothelial cells (SVEC4–10, ATCC CRL-2181, passages 10–12), mouse macrophages (RAW 264.7, ATCC TIB-71, passage 25) were cultivated in low-glucose Dulbecco's modified Eagle's medium (DMEM, Thermo Fisher Scientific Inc., MA, USA) supplemented with 10% foetal bovine serum and 1% penicillin/streptomycin. All cell types were incubated in a humidified environment at 37 °C under a 5% CO_2 atmosphere.

2.9.2. ROS induction

The generation of reactive oxygen species (ROS) by macrophages upon exposure to the surface coatings was quantified using the ROS probe 2′,7′-dichlorofluorescein diacetate (DCFDA, 50 μM). In brief, RAW 264.7 cells were seeded in a 96-well plate at a density of 1×10^4 cells per well for 4 h and subsequently cultured in DMEM medium in the presence of the coated surfaces. For comparison, control cell samples were maintained in DMEM alone without exposure to the coatings. Following a 24-h incubation under standard culture conditions, the media was removed and a volume of 100 μL of 50 μM DCFDA in PBS was added and subsequently incubated for 30 min. Finally, the fluorescence intensity (FI) was measured at an excitation peak of 485 nm and an emission peak of 535 nm using a microplate reader.

2.10. Cell viability

The cytocompatibility of the sPASP coatings was evaluated using the PrestoBlue™ (Thermo Fisher Scientific Inc., MA, USA) cell viability assay, with SVEC4–10 endothelial cells and RAW 264.7 macrophages serving as representative cellular models. SVEC4–10 and RAW 264.7

cells were seeded into 96-well tissue culture plates at densities of 8×10^3 and 1×10^4 cells per well, respectively. After an initial 24-h incubation period, PET and sPASP-coated PET samples were introduced into the wells and further incubated for 24 h at 37 °C. Control wells contained cells cultured in medium without material exposure. The PrestoBlue assay was performed in accordance with the manufacturer's protocol, and cell viability was subsequently quantified using the following equation [35]:

$$\textit{Cell viability}\ (\%) = \frac{OD_{sample} - OD_{blank}}{OD_{control} - OD_{blank}} \times 100\% \quad (3)$$

2.10.1. Cell adhesion

Cell attachment was assessed using the LIVE/DEAD™ (Thermo Fisher Scientific Inc., MA, USA) assay and visualised under a CKX53 inverted microscope (Olympus Corporation, Japan). In this experiment, a 96-well plate was coated using the same method as described in Section 2.4 and subsequently exposed to UV irradiation for sterilisation. SVEC4–10 cells were cultured at a density of 8×10^3 cells per well for a duration of 24 h. Subsequently, the samples were rinsed three times with PBS to eliminate non-adherent cells. The remaining cells were stained with calcein-AM (green fluorescence, 1 μM) and propidium iodide (red fluorescence, 1 μM), followed by observation under a fluorescence microscope. Additionally, FI was quantitatively measured to evaluate the extent of cell adhesion according to the following formula.

$$\textit{Live cell adhesion}\ (\%) = \frac{FI_{live}}{FI_{live} + FI_{dead}} \times 100\% \quad (4)$$

2.11. Platelet adhesion on sPASP coatings

Citrated whole human blood, retrieved from healthy volunteers following the guidelines set out by the Griffith University Human Ethics Committee (approval number: 2021/598), was first centrifuged at 1500 rpm for 15 min to isolate platelet-rich plasma (PRP). Subsequently, 400 μL of this PRP was applied to the surfaces of samples. Following a 2-h incubation period at 37 °C, all samples were washed three times with PBS. The adhered platelets were stained with DiOC6 at the concentration of 1 $\mu g \cdot mL^{-1}$ in PBS for 30 min at room temperature [36]. Platelets were then visualised using fluorescence microscopy. Quantification was conducted *via* two complementary methods: firstly, by measuring the FI of DiOC6 at an excitation wavelength of 482 nm and an emission wavelength of 504 nm; and secondly, by manual counting of platelet cells using ImageJ software (National Institutes of Health, USA). In the latter approach, images captured under the microscope were processed using a gating threshold of 2 μm to ensure accurate identification and enumeration.

2.12. Antithrombogenicity of sPASP coatings

We measured activated partial thromboplastin time (APTT) and thrombin time (TT) to evaluate the impact of the sPASP surface on the coagulation system. For these tests, fresh anticoagulated human blood was centrifuged at 3000 rpm for 15 min to obtain PPP. For the APTT assay, we mixed 100 μL of PPP with APTT reagent (Dade® Actin FSL, Siemens Healthineers, Erlangen, Germany) and incubated them at 37 °C for 30 min. The mixture was then applied to the surface of both PET and sPASP coatings, followed by the addition of 50 μL of 0.025 M calcium chloride, and the time taken for plasma clotting was measured manually by tilting the tubes every 15 s. For the TT assay, 100 μL of PPP was placed on the surfaces of PET and sPASP coatings, to which 50 μL of TT reagent (Dade® Thrombin Reagent, 50 $IU \cdot mL^{-1}$, Siemens Healthineers AG, Erlangen, Germany) was added at 37 °C, and the clotting time was subsequently recorded manually by tilting the tubes every 30 s.

2.13. Thrombin generation assay

To assess thrombin generation on the prepared surfaces, a systematic approach was followed. Initially, the surfaces were equilibrated with PBS at 37 °C to simulate physiological conditions. Subsequently, a solution was prepared by mixing 50 μL of 1 mM fluorogenic substrate (Boc-Val-Pro-Arg-AFC, thrombin substrate, Sigma-Aldrich, Inc., MO, USA) with 10 μL of 25 mM calcium chloride to provide necessary ions for the coagulation cascade. After the equilibration phase, the PBS was carefully removed, and 40 μL of double-centrifuged PPP was added to each surface [37]. The thrombin generation was then quantitatively evaluated by measuring the conversion of thrombin substrate using a plate reader. FI was measured using 380 nm excitation and 440 nm emission filters, which are optimal for the fluorescent 7-amino-4-methylcoumarin, a cleaved product of thrombin substrate. The intensity of fluorescence correlates with the amount of thrombin produced, providing a precise and reliable measurement of thrombin generation on the surfaces.

2.14. Antithrombogenicity of sPASP coatings under flow conditions

Under the duress of shear stress, the susceptibility of blood components, particularly those implicated in the coagulation cascade, is heightened [1,38]. In light of this, we employed two prevalent *in vitro* flow models to assess the haemocompatibility of coatings: Chandler loop and microfluidic device. The Chandler loop system utilised PVC tubing with a 5 mm inner diameter and an overall length of 50 cm, affixed to a motor rotating at an approximate 30 rpm. In parallel, the microfluidic device comprised a single-channel chip with dimensions of 20 mm in length, 255 μm in width, and 110 μm in height. A shear rate of 1000 s^{-1}, replicating physiological conditions, was achieved by setting the syringe pump to a flow rate of 31 $\mu L \cdot min^{-1}$. The setup parameters were detailed in Table S3. Both models were perfused with fresh citrated blood for a duration of three hours. The integrity and composition of the blood were analysed pre- and post-perfusion *via* six established haemofactors: erythrocytes, platelets, leukocytes, haematocrit, haemoglobin concentration, and haemolysis rate. Leveraging the transparency of the microfluidic device, direct microscopic observations were made. Platelets were labelled with DiOC6 at a concentration of 1 $\mu g \cdot mL^{-1}$, similar to the previously described conditions (section 2.10), facilitating real-time visualisation and documentation of platelet adhesion within the microfluidic channels. This multi-faceted approach provides a robust framework for investigating the performance of sPASP coatings, our candidate of interest, under flow conditions that simulate the vascular environment.

2.15. Antibacterial adhesion of sPASP coatings

Surface coatings were placed into a 96-well plate and bare PET sheet served as the control. Kanamycin at a concentration of 0.01 $mg \cdot mL^{-1}$ was used as positive control for bactericidal efficacy. 100 μL of bacterial suspension (*E. coli* and *S. aureus*) with OD of 0.2 was added to the wells. The wells were incubated at 37 °C and stirred at 200 rpm for a period of 1.5 h, facilitating uniform bacterial exposure to the surfaces. Subsequently, the suspension was transferred to new wells for OD measurement at 600 nm, which serves as an indirect quantification of bacteria. The surfaces were gently rinsed once with PBS to remove non-adherent bacteria. For quantifying bacterial adherence, alamarBlue™ (Thermo Fisher Scientific Inc., MA, USA) cell viability reagent, diluted in broth at a 1:9 volume ratio, was employed. This reagent is a cell viability indicator that measures the metabolic activity of attached bacteria. The alamarBlue-incubated mixture was then pipetted into fresh wells, and absorbance was measured at 570 nm.

2.16. Stability of sPASP coatings

To ascertain the resilience of the coatings, we subjected them to

durability tests, utilising both chemical and mechanical stressors. Specifically, PASP, sPASP40, and sPASP80, were systematically analysed. For chemical resistance, the coated surfaces were placed into Eppendorf tubes filled with either PBS or PPP. The functional group density and WCA were meticulously quantified before and after immersion at designated intervals of 1, 7, 10, and 14 days. With PPP, the solutions were refreshed daily to closely replicate the dynamic plasma environment of the bloodstream. Mechanical endurance was probed through exposure to ultrasonic waves. The coatings were immersed in water within an ultrasonic bath set to maximum intensity. The assessment of functional group density and WCA was repeated at specified durations pre- and post-sonication at 15, 30, 45, and 60 min, providing a comprehensive evaluation of the coatings' stability against acoustic stress [3]. This dual approach to durability testing is essential to predict the long-term performance of sPASP coatings in clinical scenarios.

2.17. In vivo inflammatory response

2.17.1. Subcutaneous implantation

The animal experiment in this study was conducted in accordance with the Guidelines for the Care and Use of Laboratory Animals of Griffith University (Approval number ESC/03/24/AEC). Healthy adult female C57BL/6 mice (weighing 18–21 g) were acquired for implantation procedures. In brief, a subcutaneous pocket approximately 0.5 cm in length was created on the dorsal region of each mouse. Bare and optimal coated PET discs (sPASP40), each with a diameter of 6 mm, were subsequently implanted into this pocket (1 disc per pocket per mouse) for a duration of 7 days. The surgical site was carefully closed using nylon sutures (Ethicon, Inc., NJ, USA). Following this period, the skin area in contact with the implant was excised and fixed in 4% paraformaldehyde for subsequent histological analysis [39]. The analysis was conducted using five mice per treatment group ($n = 5$).

2.17.2. Histological procedures

Following fixation, specimens were embedded in cryomoulds filled with Tissue-Tek O.C.T. Compound (Sakura Finetek Japan, Tokyo, Japan) and rapidly frozen in liquid nitrogen. Longitudinal sections with a thickness of 6 μm were subsequently stained using haematoxylin and eosin (H&E) for both morphological and morphometric evaluation. In addition, sections were mounted on silanised slides (Superfrost) for immunohistochemical (IHC) staining targeting alpha-smooth muscle actin (α-SMA, Cat. ab184675) and CD163 (Cat. ab313666) supplied by Abcam plc (Cambridge, UK) with the same dilution ratio of 1:100 for 24 h.

2.17.3. Capsule thickness measurement

The specimens were captured using bright-field microscopy at a magnification of 10×. ImageJ was employed to quantify the average capsule thickness within each group. These measurements were subsequently compared to untreated skin samples obtained from healthy mice as a control.

2.17.4. Numerical density of leukocytes

The number of inflammatory cells was estimated within both the capsule region and the adjacent tissue. Quantification was performed on five H&E-stained sections using a standardised field area of 0.31 mm^2. Within each field, inflammatory cell types, including neutrophils, lymphocytes, plasma cells, and macrophages, were counted using ImageJ, applying a diameter gating range of 15–30 μm and a circularity range of 0.2–1.0. The results were statistically compared with those of the control group [39].

2.17.5. Inflammatory reaction score

The inflammatory response within the capsule was evaluated based on both the number and distribution of inflammatory cells. Each implant was scored according to the following classification: 0 – absence of inflammatory infiltrate (few inflammatory cells); 1 – mild infiltrate; 2 – moderate infiltrate; and 3 – severe or intense infiltrate. The assessment was conducted across five mice per group, and the mean score for each group was subsequently calculated [39,40].

2.18. Statistical analysis

Each sample was subjected to a minimum of three independent experiments ($n \geq 3$), and the results were expressed as the mean (± standard deviation, SD). Statistical evaluations were carried out utilising GraphPad Prism software (GraphPad Software, LLC, USA), with a p-value of less than 0.05 deemed statistically significant. In addition, each data set was analysed, and significance was denoted as ns ≥ 0.05, $^{*}p < 0.05$, $^{**}p < 0.01$, $^{***}p < 0.001$, $^{****}p < 0.0001$. The heat map presented in Fig. S7 was constructed by normalising the results of each sample for every parameter on a scale from 0 to 100. In this scale, red indicated a detrimental effect, whereas yellow reflected a beneficial one. The sample that achieved the most favourable overall profile across these parameters was then selected as the optimal formulation.

3. Results and discussion

3.1. Characterisation of PSI and PASP

In this study, PASP was derived from its precursor, PSI, which was synthesised *via* a condensation reaction of *L*-aspartic acid in a sulfolane solvent catalysed by phosphoric acid. The subsequent generation of PASP was achieved through the alkaline hydrolysis of PSI by sodium hydroxide. The synthetic pathways for both polymers were illustrated in Fig. S1A. While PSI was characterised by repeating succinimide monomer units, its hydrolysed derivative, PASP, was defined by aspartic acid residues linked *via* amide bonds. Verifying the chemical structures of these polymers not only confirmed the successful synthesis but also served as reference spectra for the subsequent characterisation of surface-coated materials.

The FTIR spectra for PSI and PASP showed distinct absorption bands reflecting their structures (Fig. S1B). PSI's FTIR spectrum exhibited significant troughs at 1792 and 1706 cm^{-1}, corresponding to the asymmetrical and symmetrical carbonyl of cyclic imides, respectively. The band at 1630 cm^{-1} is indicative of stretching vibrations of carbonyl in amide band I. Post-hydrolysis, PASP formation was marked by a new intense overlapping band between 1580 and 1630 cm^{-1}, indicating stretching signal of C═O (amide band I) and a mixed vibration of N—H bending and C—N stretching (amide band II). The hydroxyl bending vibrations at 1391 cm^{-1} was also observed. In addition, the ^{1}H NMR spectra of PSI and PASP both displayed characteristic peaks of the materials, as shown in Fig. S1C. Specifically, the ^{1}H NMR spectrum of PSI exhibited a distinctive peak at a chemical shift of 5.27 ppm, along with two symmetrical peaks at 3.21 and 2.71 ppm. In contrast, the PASP spectrum showed two characteristic multiplets at 4.37 and 2.68 ppm. The consistency of these findings with our group's previously reported studies further confirmed the successful synthesis of the precursors used for the coating layer [26–29].

3.2. Characterisation of sPASP coatings

The composition of the sPASP coatings is delineated in Fig. 1 A, employing a strategy where a PDA intermediary layer was included and crucial for reinforcing the interface between the sPASP coating and the PET substrate. In particular, PASP was covalently linked to PDA-coated PET surface and simultaneously sulfated by a sulfating agent AHS. This is a one-pot reaction mediated by EDC coupling reaction. The resultant surface was named sPASP. Different contents of AHS were used to adjust the sulfation degree of PASP (0%, 10%, 20%, 40%, 60%, 80% input molar ratio of AHS:PASP monomer). The ratios of reactants were detailed in Table S1 and the resultant coatings were denoted as PASP,

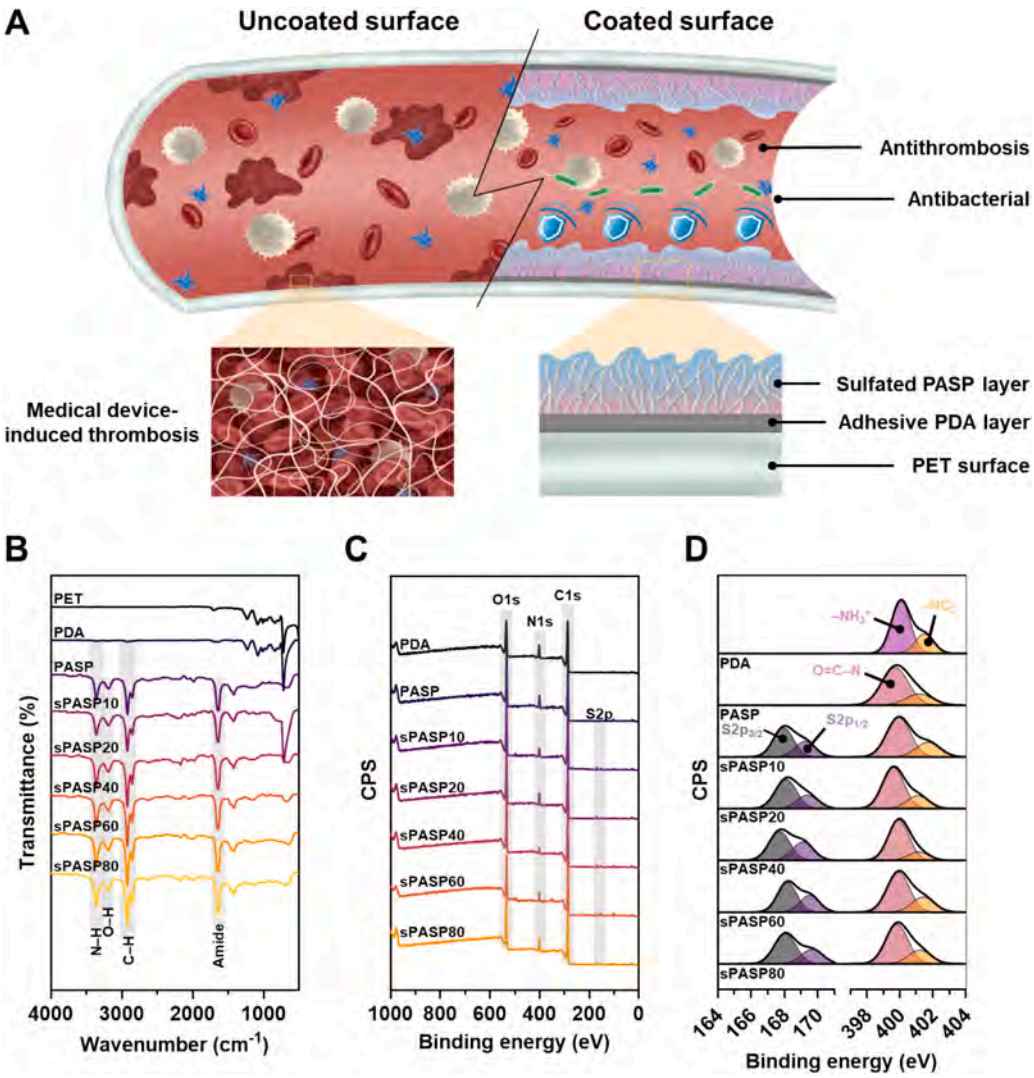

Fig. 1. Chemical characterisation of PET, PDA, and sPASP coatings. (A) Illustration of sPASP coating *via* PDA adhesive layer on PET surface and its surface anticoagulant and antibacterial capabilities. (B) FTIR spectra. (C) X-ray photoelectron spectroscopy survey scans, and (D) high-resolution spectra of N1s and S2p of PDA, sPASP coatings.

sPASP10, sPASP20, sPASP40, sPASP60, sPASP80, respectively. The intrinsic sulfation and highly negative net charge of sPASP coatings were designed to maintain biocompatibility at the surface, effectively reducing biomolecule adhesion and diminishing blood interaction. Furthermore, the incorporation of a sulfation sequence along the sPASP polymer backbone was inspired by the characteristic structural features of heparin or heparan sulfate, which motivated the introduction of sulfate groups into PASP. This modification aimed to enhance antithrombin activity and consequently reduce the thrombogenicity of foreign surfaces upon contact with blood.

We performed a comprehensive analysis of these surface coatings, including chemical, morphological, and physical characterisations. In this context, techniques such as FTIR and XPS spectroscopy are invaluable for elucidating the molecular composition and surface reactivity of these coatings. As depicted in Fig. 1B, all samples displayed peak patterns consistent with the base PET substrate, but with decreased intensity as the sulfation level increased. Moreover, there was a noticeable increase in absorption intensity around 3350 cm^{-1}, suggesting the presence of O—H and N—H bonds in the PDA coatings. For the sPASP coatings, a significant overlapping absorption near 1670 cm^{-1} was evident, which can be attributed to the amide I and II bands of PASP, a feature distinguishing it from the PDA. Additionally, the emergence of a doublet at 1460 and 1410 cm^{-1}, corresponding to the O—H bending and S═O stretching vibrations, was indicative of the carboxyl and sulfate groups in the PASP and sPASP coatings. This aspect underscores the successful integration of the sPASP onto the PDA-modified PET surface. These spectroscopic observations preliminarily confirm the presence of the sPASP hydrogel coatings on the PDA surface.

The XPS analysis shown in Fig. 2C and D identified carbon and oxygen as the primary elements on the PET substrate, while the introduction of the sPASP coating was marked by the emergence of nitrogen (N1s) and sulfur (S2p) peaks. The N1s peak, characteristic of the amide groups in sPASP, displayed prominently at around 400.5 eV. Deconvolution of the N1s peak showed that the PDA nitrogen signal mainly appeared at 401.7 eV, a range associated with higher-level amines, indicating a greater presence of free amine groups or cyclised indole-type structures. In contrast, the N1s peaks of the PASP and sPASP shifted towards lower binding energies at around 400.3 eV, suggesting the formation of amide groups following the introduction of the poly(amino acid) [41]. At the same time, the proportion of free amino groups tended to decrease. Moreover, the distinctive S2p peak appeared at 168.0 eV, confirming the presence of sulfate groups. However, the elemental analysis presented in Table 1 revealed a discrepancy in sulfur content. While the sulfur content increased gradually from 0% in PASP to 1.18%

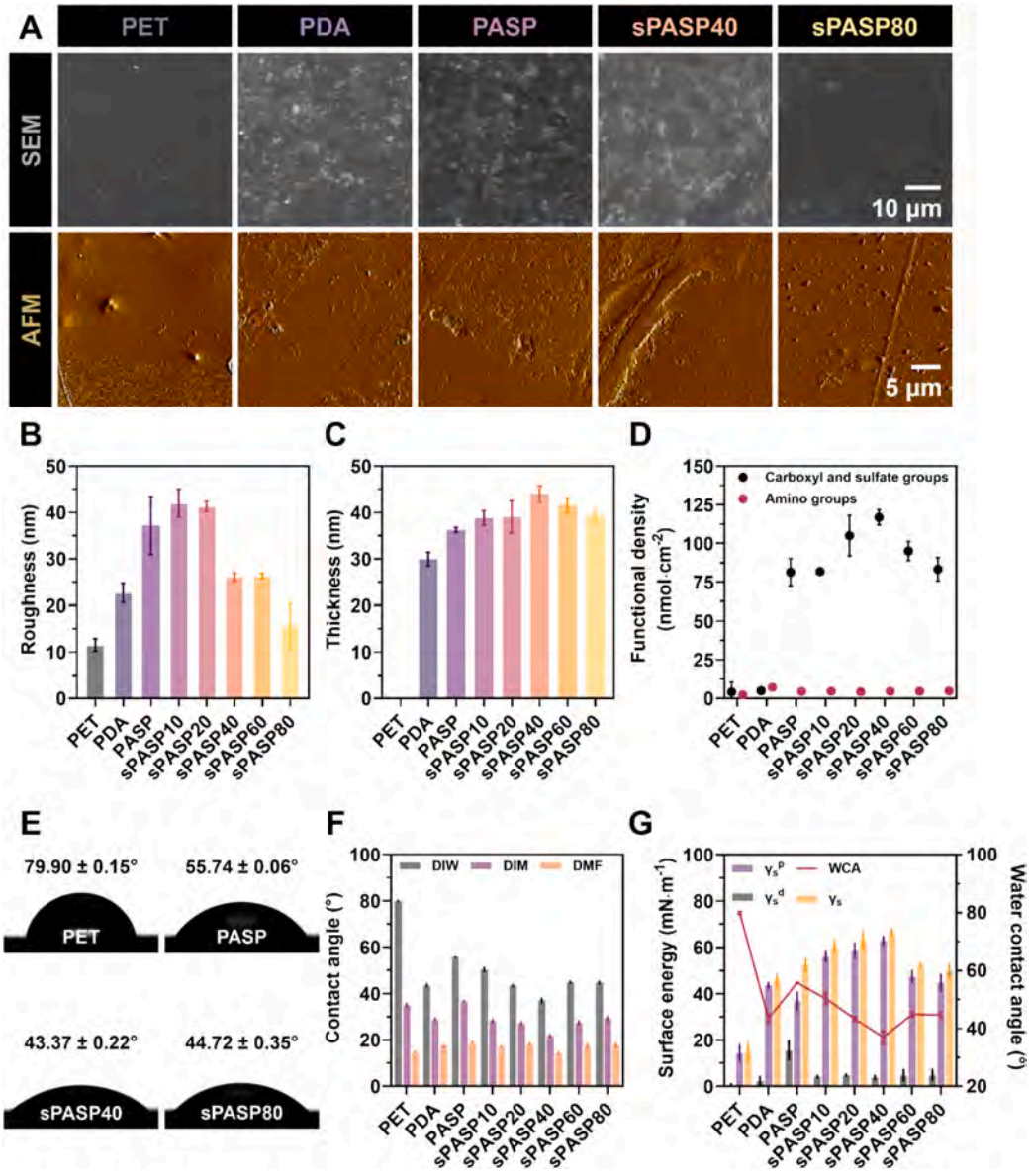

Fig. 2. Surface characteristics of sPASP coatings. (A) Representative images taken by SEM and AFM patterns, (B) roughness and (C) thickness parameters of plain PET, PDA, sPASP surface coatings. (D) Comparison of functional groups including negative- and positive-charged groups evaluated by TBO and AO II assay, respectively. (E) Photos of water droplets on (i) pristine PET, (ii) PASP, (iii) sPASP40, and (iv) sPASP80. (F) Measurement of contact angles using different liquids: DIW, DIM, and DMF. (G) Liquid surface tension and its components (polar and dispersive components) compared to WCA, indicating the lower contact angle the higher surface energy of surfaces.

Table 1
Atomic concentrations of sPASP coatings from XPS survey scans

	Elements (atom %)			
	C1s	N1s	O1s	S2p
PDA	73.65	8.83	17.52	0
PASP	69.65	7.04	23.32	0
sPASP10	69.72	4.94	24.95	0.38
sPASP20	69.24	4.81	25.03	0.92
sPASP40	69.12	3.17	26.54	1.18
sPASP60	69.53	7.03	23.01	0.42
sPASP80	69.36	7.25	22.99	0.39

in sPASP40, there was a notable decline in sPASP60, continuing to decrease to 0.39% in sPASP80. This reduction contrasted with the trend in N1s intensity, indicating a reduced coverage of sPASP and the resulting exposure of the underlying amino-rich PDA substrate. This likely arises from competitive kinetics between the PASP backbone, AHS, and PDA. Because of its low molecular weight, AHS reacts more quickly with the carboxyl groups on the PASP chains. In contrast, higher-molecular-weight PASP interacts less effectively with the PDA surface, resulting in lower coating density as more AHS is added, and thus lower sulfur content. Nonetheless, these findings still highlight the formation of a thin sPASP layer, supported by the highly reactive PDA coating on the PET substrate.

3.3. Surface characteristics of sPASP coatings

Physical surface properties are pivotal in mediating the interactions of biomaterials with their biological environments, affecting cell adhesion, proliferation, and overall biocompatibility. The surface morphology of sPASP coatings was thoroughly analysed using SEM and AFM. As shown in Fig. 2 A and S2, the uncoated PET surface is characterised by its smoothness, with an average roughness (R_q) around 11.5

± 1.1 nm (Fig. 2B). In contrast, the PDA-coated PET surface showed a distinct topographical change due to PDA self-polymerisation, resulting in a granular pattern made of PDA particles. After sPASP coating, a significant escalation in surface roughness was observed, although no discernible visual change was apparent in PASP, sPASP10, and sPASP20, with respective R_q values of 37.2 ± 5.1 nm, 42.0 ± 2.4 nm, and 41.3 ± 0.9 nm, respectively. This increase in roughness is indicative of the polymer fibres being superposed onto the granular layer of PDA. Interestingly, with augmented sulfation, the roughness notably diminished for sPASP40, sPASP60, and sPASP80, as evident in the SEM and AFM images (Fig. 2 A and S2). Correlating these findings with the coating thickness measurements (Fig. 2C), the PDA layer exhibited a thickness of 22.7 ± 1.7 nm. In contrast, coatings incorporating PASP and sPASPs showed a marked increase in thickness, with sPASP40 reaching a maximum of 44.0 ± 1.4 nm. This significant increase compared to the PDA layer highlights the effectiveness of the sPASP coating process.

The observed variation in roughness across the sPASP coatings can be attributed to the competitiveness of two primary reactions during the coating process: (1) the conjugation of PASP to the PDA layer and (2) the conjugation of AHS to the PASP structure. Given that one-pot synthesis combines all reactants at once, both reactions are plausible. At lower AHS concentrations, PASP molecules are more likely to react with the amino groups on PDA, leading to an accumulation of PASP and sPASP chains on the PDA granules and thus, an increase in the roughness of PASP, sPASP10, and sPASP20. Conversely, at higher AHS concentrations, AHS molecules, due to their smaller molecular weight, competitively react with the PASP chains first. This results in a reduction of active functional groups (carboxyl) on the polymer chain, and thereby a more controlled and even deposition and attachment of polymer chains onto the PDA. This suggests that sPASP coatings with higher sulfation degrees are likely to facilitate more regulated interactions due to their lower roughness, potentially minimising trigger and degradation of blood components, particularly proteins and platelets. The enhanced thickness of the sPASP coatings further suggests a heightened biological activity associated with these coatings.

The biological efficacy of synthetic sulfated polymers is notably influenced by their degree of sulfation, as well as the presence and density of surface functional groups, which play a vital role in their interactions with blood components and cellular compatibility. Consequently, the quantification of functional group densities, such as carboxyl, sulfate, and amino groups, was carried out employing staining methods using TBO for negatively charged groups and AO II for positively charged groups. According to the results presented in Fig. 2D, compared to negative-charge groups, the content of primary or secondary amino groups across all coatings was low. PDA coating exhibited the highest amino group density, measured at 7.1 ± 0.6 nmol·cm^{-2}. All sPASP coatings exhibited similar amino group density, approximately 4.5 nmol·cm^{-2}, which was much lower than PDA coating. This is probably due to the conjugation of PASP to PDA which reduced the number of primary amine groups. The data further demonstrated the successful conjugation of PASP to PDA. Regarding negatively charged groups (Fig. 2D), both PET and PDA surfaces exhibited minimal density of these groups. In comparison, the PASP and sPASP coatings displayed a substantial increase in the density of negatively charged groups, corroborating the success of the coating process. An intriguing correlation was observed with surface roughness, wherein the functional group density peaked at 116.8 ± 1.6 nmol·cm^{-2} for sPASP40 and then declined to 83.2 ± 2.5 nmol·cm^{-2} for sPASP80.

Relative to the PDA-coated sample, PASP- and all sPASP-coated surfaces exhibited a reduced surface amino content due to the conjugation of PDA amino groups with PASP carboxyl groups, with an average of 36.2% of amine groups conjugated along the PASP chain. This consistency indicates that carboxyl conjugation did not change significantly across PASP and sPASP coatings. Thus, the variations observed in the TBO-assay results, particularly the increased negative charge of sPASP20 and sPASP40 relative to PASP, stem from an increase in the sulfate group content. This confirms successful sulfation, with the sulfation efficiency reaching an optimum at 40% AHS relative to succinimide units (sPASP40). However, further increases in AHS concentration led to a decrease in negative charge groups. This trend can be explained by the competitive reactions during the coating process among PASP backbone, AHS, and PDA. Due to its low molecular weight, AHS exhibited a faster reaction rate with the carboxyl groups along the PASP backbone. This reduced the reactivity of PASP towards PDA due to a decrease in available carboxyl groups, which in turn led to a lower coating density as the AHS content increased. Additionally, the increased sulfate group content enhanced electrostatic repulsion, further contributing to the reduced coating density. The reduced coating density corresponded to fewer sPASP molecules on the surface, resulting in a lower negative charge (less sulfate groups) compared with the sPASP40 sample.

In addition to the aforementioned surface and physical attributes, surface wettability emerges as a crucial characteristic in the realm of biological coatings. Hydrophilic surfaces are capable of forming a hydration layer, acting as a barrier to minimise undesirable interactions with blood components [35,42]. Consequently, we assessed the hydrophilicity and computed the surface energy of each sPASP coating. Primarily, WCA serves as an appropriate metric for evaluating surface wettability. As depicted in Fig. 2E and F, the PET substrate, characterised by its aromatic ring and dimethylene block composition, exhibited a notably high WCA of 79.90 ± 0.15°, bordering on hydrophobicity. The application of PDA and subsequent sPASP coatings resulted in a significant decrease in WCA, indicative of enhanced wettability and increased surface energy. Notably, sPASP40 demonstrated the lowest WCA at 36.96 ± 0.71°, aligning with expectations given the abundance of active functional groups, such as catechol and amino in PDA, and carboxyl, sulfate, and amide linkages in sPASP coatings. These groups facilitate hydrogen and ionic bonding with water molecules during hydration, leading to improved antifouling properties compared to the uncoated PET surfaces. Moreover, to ascertain the SFE of the coatings, contact angle measurements were also performed with solvents such as DIM and DMF, as represented in Figs. 2F and S3. The use of water and DIM, representing polar and dispersive solvents respectively, aids in accurately determining surface tension, while DMF serves to validate the accuracy of these measurements, as evidenced in Table S2. Fig. 2G demonstrates that there exists a strong correlation between surface energy and WCA; a lower WCA correlates with higher SFE, and *vice versa*. The determination of both contact angle and SFE is integral to the analysis of coating materials. Furthermore, SFE is a key driver between materials and biological interaction.

3.4. Biocompatibility of sPASP coatings

Biocompatibility, particularly interaction with cells, blood components, and immune system, is highly important in biomedical applications. This ensures that the materials do not induce adverse reactions such as inflammation, cytotoxicity, or haemolysis which could compromise their efficacy and patient safety. For blood-contacting implants or devices like stents or catheters, maintaining erythrocyte integrity and avoiding haemolysis is crucial to prevent anaemia or adverse thrombosis. In this study, the erythrolytic potential of various surface coatings was assessed through their exposure to a RBCs suspension, followed by incubation at 37 °C for 24 h. Triton X-100 was used to induce RBC lysis and thus served as a positive control, while PBS was employed as a negative control. As shown in Fig. 3 A, all coatings did not significantly lyse RBCs with haemolysis percentages were all below 5%, a threshold generally considered acceptable in clinical evaluations concerning erythrolytic activity. Notably, PASP, sPASP10, sPASP20 and sPASP40 were slightly better than PET, PDA, sPASP60, and sPASP80 in terms of haemocompatibility. This can be attributed to certain surface functionalities known to disrupt red blood cells. These include

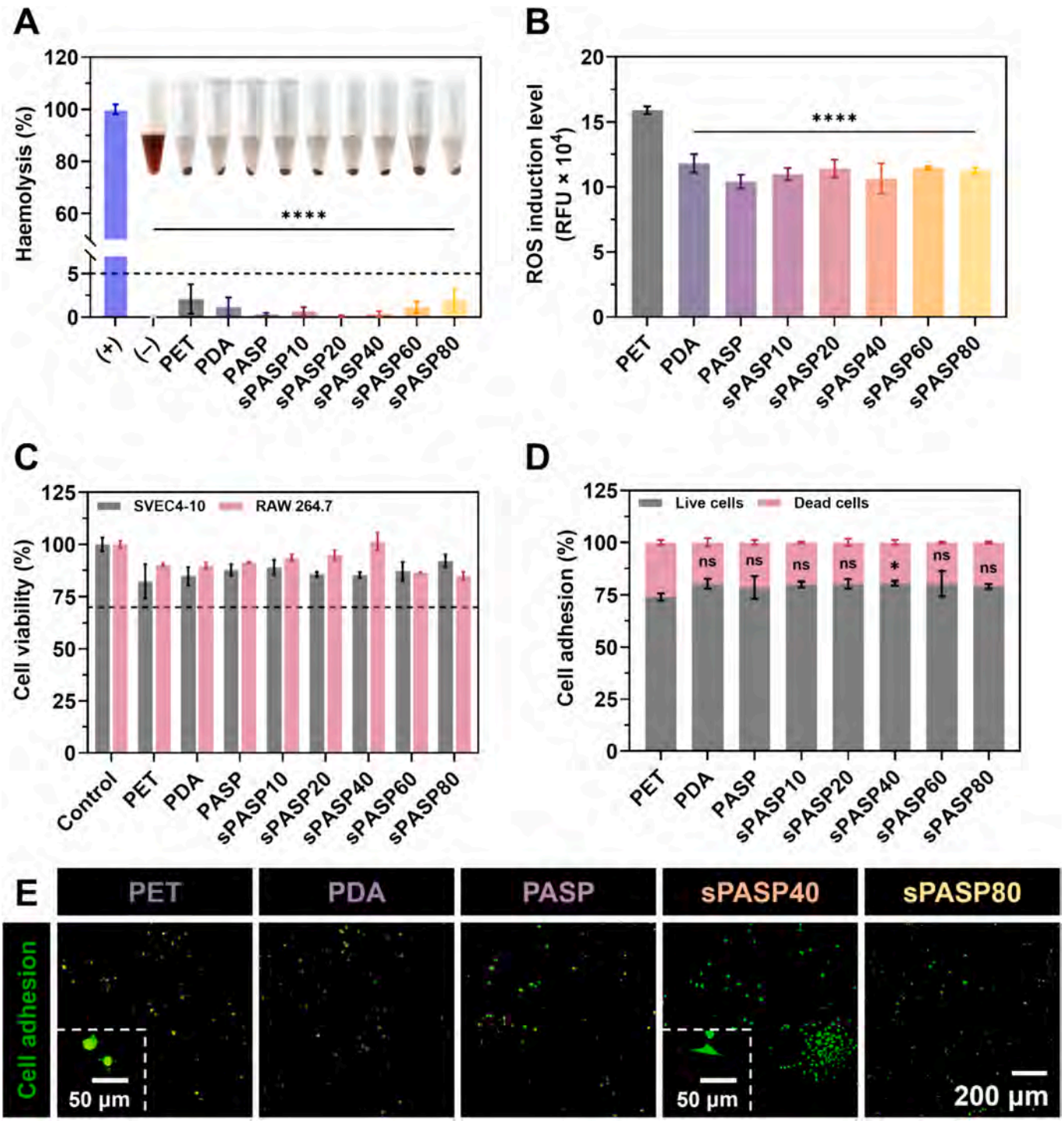

Fig. 3. Evaluation of biocompatibility and SVEC4–10 cell adhesion on sPASP coatings. (A) Quantitative analysis of haemolysis percentage upon contact with sPASP coatings and inset representation of the experimental results (in sequential order from left to right). (B) Measurement of ROS level induced in macrophages following co-culture with sPASP coatings. (C) Cell viability assessment using PrestoBlue reagent for SVEC4–10 endothelial cells and RAW 264.7 macrophages exposed to surface coatings over 24 h. (D) Evaluation of SVEC4–10 adhesion on sPASP coatings using LIVE/DEAD staining after 24 h. (E) fluorescence imaging live cell adhesion.

hydrophobic properties and positively charged surfaces, both of which can compromise the integrity of RBC membranes. Hydrophobic interactions may destabilise the phospholipid bilayer of RBCs, and surfaces with positive charges can interfere with the negatively charged membranes, leading to haemolysis.

Assessing cell viability upon contacting surface coatings is crucial in biomedical applications, as it indicates whether the surface is non-toxic and compatible with living cells. High cell viability suggests that the coating supports or at least does not adversely affect key cellular functions like growth, attachment, and proliferation. In blood-contacting devices such as blood tubing, material compatibility with endothelial cells must be evaluated, as these cells constitute the monolayer lining the interior of blood vessels and are thus frequently in contact with such devices. Additionally, macrophages play a significant role in interacting with foreign materials introduced into the body. Consequently, SVEC4–10 endothelial cells and RAW 264.7 macrophages were selected

as representative cell types for assessing cytocompatibility. As depicted in Fig. 3C, both cell types exhibited high viability, above 80%, after a 24-h culture period directly on the surface of the tested coatings, underscoring their compatibility with cellular components. Similarly, minimising ROS induction is vital to prevent oxidative damage to surrounding tissues, which can lead to chronic inflammation or even failure of the implant. Furthermore, inflammation triggers blood clotting as a protective mechanism, in which the inflammatory response activates platelets and the coagulation cascade to form clots. DCFDA was employed to evaluate the redox state of macrophages cultured in the presence of different sPASP coatings. The findings (Fig. 3B) indicate that the coating with PDA, a material renowned for its high biocompatibility, resulted in a significant reduction in ROS production. Specifically, the ROS levels in cells cultured on PDA-coated PET surface were measured at 11.8 ± 0.6 relative fluorescence units (RFU) $\times 10^4$, compared to 15.9 ± 0.2 RFU $\times 10^4$ on pristine PET surface. Similarly, the sPASP coatings demonstrated efficacious ROS reduction, with the lowest ROS levels observed at 10.4 ± 0.4 RFU $\times 10^4$ for the PASP coating. It was observed that all sPASP-coated surfaces exhibited lower ROS production by macrophages compared to the PDA surface, indicating a potential for reduced oxidative stress in a biological context.

Cell adhesion is crucial for the long-term performance of blood-contacting medical devices. Adequate cell adhesion promotes endothelialisation, a process where endothelial cells cover the device surface, forming a biocompatible interface that mimics the natural lining of blood vessels. This endothelial layer is essential for preventing further complications such as thrombosis, inflammation, and immune responses, thereby enhancing the device's longevity and functionality in the body [16,43]. In this study, SVEC4–10 cells were seeded on top of coating layers, cultured for 24 h and washed thorough with fresh media. The adhesion of endothelial cells was visualised by staining cells with LIVE/DEAD reagents. As shown in Fig. 3E and S4 while some cell adhesion was observed on unmodified PET substrates, the cells often appear unhealthy and tend to adopt a spherical morphology (as shown in insets of Fig. 3E), indicating suboptimal conditions. In addition, the percentage of viable cells (Fig. 3D) was notably higher on coated surfaces, indicating enhanced biocompatibility and improved cell adhesion. Among the tested surfaces, sPASP40 exhibited a statistically significant enhancement in cell attachment, reaching $80.6 \pm 0.9\%$, whereas the unmodified PET surface showed a lower viability of only $74.1 \pm 1.5\%$. The results highlighted a marked improvement in cellular health, as evidenced by the presence of elongated and relaxed morphologies, which are characteristic of more favourable interactions between the endothelial cells and the coating. Enhanced adhesion of endothelial cells on these surfaces also suggested the potential for promoting neo-endothelialisation, thereby facilitating more rapid integration of coated implants into host tissue while minimising adverse physiological responses.

3.5. Anti-biofouling performance of sPASP coatings

Anti-biofouling properties are essential to prevent surface-induced thrombosis because they minimise the accumulation of proteins, cells, and other biological materials on the surface of medical devices [1,44]. This accumulation can activate the coagulation cascade and platelets, leading to blood clot formation [45,46]. Anti-biofouling surfaces help maintain a clean interface that resists such undesirable adhesions, thereby reducing the risk of thrombosis [1,32]. In the context of blood-contacting implants, the initial non-specific adsorption of proteins upon exposure to blood plays a pivotal role in triggering thrombosis, potentially leading to implant failure [22,47]. This study utilised BSA and FBG as representative protein models, given their significant influence on blood coagulation. BSA is recognised for its anticoagulant properties, whereas FBG is known to activate platelets, initiate the coagulation cascade, and facilitate thrombosis upon adsorption [48]. Additionally, 10% PPP was employed to mimic the interaction between serum plasma and the implant surface. Uncoated PET substrates exhibited considerable protein adsorption in all experiments (Fig. 4 A). Similarly, PDA coating demonstrated a substantial capacity for protein adsorption, with FBG adsorption recorded at $30.03 \pm 1.05\ \mu g \cdot cm^{-2}$ and BSA adsorption at $39.56 \pm 1.45\ \mu g \cdot cm^{-2}$. This propensity can be attributed to the fact that both proteins possess an isoelectric point (pI) of approximately 5.5, causing them to bear a negative charge at physiological pH. The surface roughness and increased area of the PDA granular surface further enhance the potential for protein binding. In contrast, sPASP coatings exhibited a reduction in protein adsorption up to two-fold compared to bare PET and PDA surfaces. This decrease in adsorption across all three protein models suggests a correlation between anti-fouling properties and surface free energy, particularly concerning wettability and the solvation of sPASP *via* hydrogen bonding and ionic solvation. The results were regarded as somewhat superior to those previously reported for sulfated alginate-based coatings [19]. However, it is important to acknowledge that this comparison remains indicative, owing to variations in experimental conditions and the nature of the substrates employed for coating.

Given the critical role of platelets in the coagulation cascade, their adhesion capacity on these surfaces was also assessed. As depicted in Fig. 4D and S5 the uncoated PET surface was extensively populated with platelets, in contrast, significantly fewer platelets adhered to the surfaces of sPASP coatings. For quantitative evaluation, platelets adhering to the surface were stained using DiOC6, emitting a green fluorescence, and analysed through two complementary methodologies to ensure correlation and accuracy: (1) measuring the FI attributed to the DiOC6 dye on the adhered platelets (Fig. 4B), and (2) counting the adherent platelets using a fluorescence microscope across four randomly selected fields (Fig. 4C). The outcomes derived from both analytical approaches were in agreement, consistently indicating that the sPASP40 sample exhibited superior antiplatelet properties. Accordingly, the morphology of platelets adhering to the PET surface and to sPASP40 was further examined using SEM, as shown in Fig. S6. The platelets on PET typically displayed a rounded form with surface projections resembling pseudopods and filopodia. In contrast, the sPASP40 coating showed markedly fewer adhered platelets, which largely retained their smooth, flat, disc-like appearance, indicating an absence of activation when compared with PET. These findings not only validate the effectiveness of these specific coatings in mitigating platelet adhesion but also underscore the robustness of the employed quantitative techniques in assessing the anti-thrombogenic potential of biomaterial surfaces.

3.6. Antithrombogenicity of sPASP coatings

The anticoagulant efficacy of the sPASP coatings was assessed through measurements of APTT and TT. APTT is widely recognised as a crucial diagnostic tool for evaluating the performance of the intrinsic coagulation pathway, offering insights into the function of several clotting factors. TT, on the other hand, is instrumental in assessing the activity of fibrinolytic systems, particularly focusing on the conversion of fibrinogen to fibrin by thrombin. As depicted in Fig. 4E, the APTT value for pristine PET was 44.0 ± 2.2 s, whereas for the sPASP-coated surfaces, particularly the sPASP40 variant, a notable prolongation in APTT was observed, reaching 140.3 ± 3.4 s, which is also more prolonged compared to sulfated alginate coatings [19]. This extension in coagulation time is indicative of a delay in the intrinsic pathway's clot formation process.

In the TT assay (Fig. 4F), pristine PET demonstrated the quickest clot formation at 23.3 ± 2.1 s. The TT value for sPASP-coated surfaces extended significantly, recorded at 62.3 ± 2.1 s for sPASP40 coatings. This result indicated that a higher coating density, and more specifically an increased presence of functional groups, especially sulfate groups, contributed to enhanced surface anticoagulant performance. While the TT values observed in sPASP60 and sPASP80 exhibited a slight decrease relative to sPASP40, the capacity for delaying coagulation remained

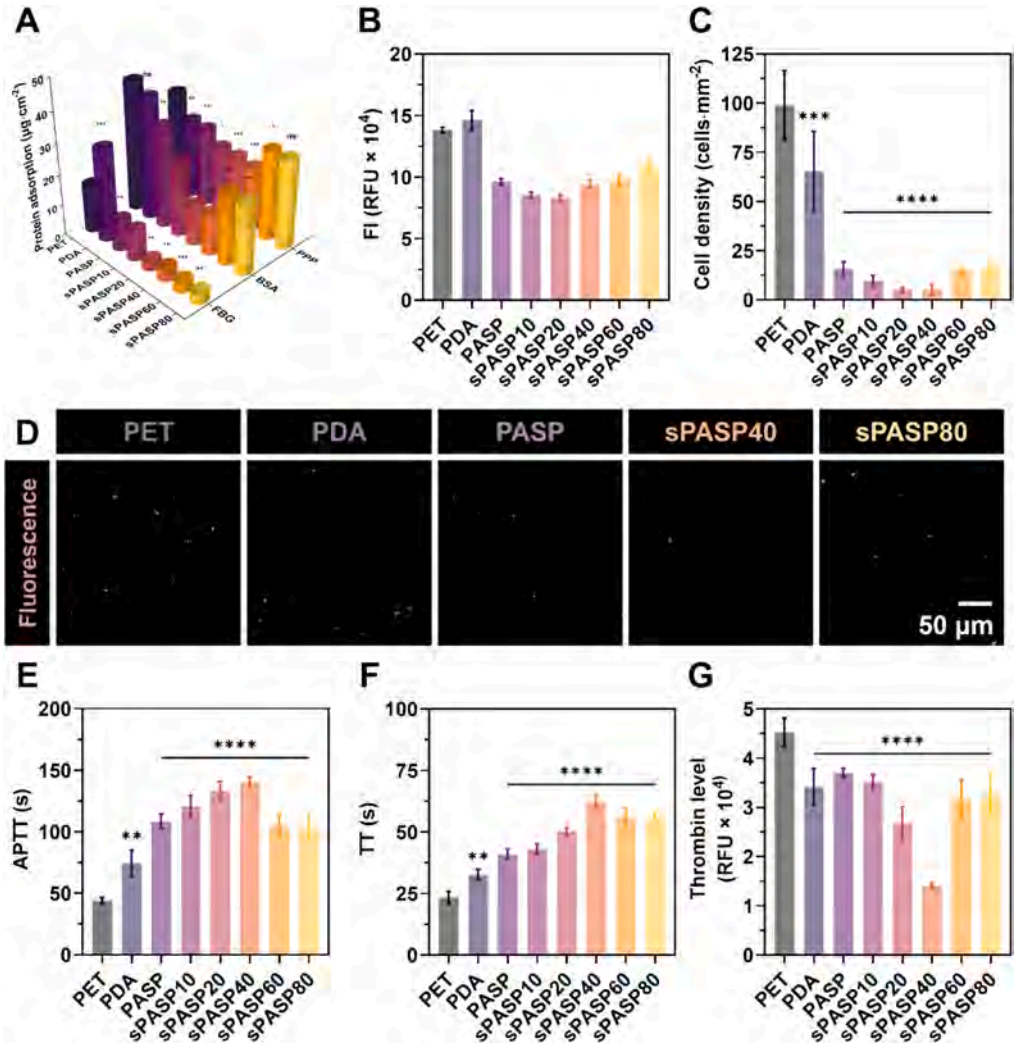

Fig. 4. Evaluation of protein adsorption, platelet adhesion, and antithrombogenic properties of sPASP coatings. (A) Analysis of protein adsorption employing FBG, BSA, and 10% PPP as model protein systems. (B) Quantification of platelet adhesion on sPASP coatings, determined *via* FI measurements of DiOC6-stained platelets. (C) Counting of bound platelets at four random microscopic fields. (D) Visualisation of platelet adhesion captured by fluorescence microscopy and SEM. Assessment of coagulation times: (E) APTT and (F) TT. (G) Measurement of thrombin generation levels following a 2-h incubation period in PPP.

markedly effective. This suggests that, despite their comparatively lesser anti-biofouling proficiency, coatings with higher sulfate content, such as sPASP60 and sPASP80, may possess enhanced capabilities to activate antithrombin. This activation plays a crucial role in moderating the action of thrombin in the conversion of fibrinogen to fibrin, a key process in the coagulation cascade [1]. The elevated sulfate levels in these coatings could thus be a contributing factor to their pronounced anticoagulant properties, indicating their potential utility in applications where mitigating thrombogenic responses is critical.

To elucidate the sulfation-dependent antithrombin activation properties of sPASP coatings, the thrombin generation assay is employed, offering an in-depth perspective on both the initiation and propagation phases of thrombin formation. As illustrated in Fig. 4G, uncoated PET samples exhibited the highest thrombin production, with a value of 4.52 $\pm$ 0.10 RFU $\times$ 10^4. Conversely, sPASP coatings demonstrated a capacity to delay thrombin formation, yielding around 3.50 RFU $\times$ 10^4. Notably, sPASP20 and sPASP40 emerged as particularly effective variants, significantly inhibiting thrombin formation with fluorescence absorbance values recorded at 2.67 $\pm$ 0.11 and 1.41 $\pm$ 0.02 RFU $\times$ 10^4, respectively. This indicates a substantial modulation of thrombin production by these coatings. For sPASP60 and sPASP80, although the reduction in thrombin levels was less pronounced, at 3.17 $\pm$ 0.12 and 3.27 $\pm$ 0.13 RFU $\times$ 10^4 respectively. This finding suggests that the sulfation level on the sPASP surface coatings plays a pivotal role in the antithrombin process. However, it is also observed that as the degree of sulfation increases, leading to a lower polymer density, there is a corresponding decrease in anticoagulant efficacy. These results collectively underscore the impact of sulfate content and polymer density of sPASP coatings on their antithrombogenic properties, highlighting the intricate balance required in optimising such coatings for clinical applications.

3.7. Stability of sPASP coatings

In this investigation, the durability of sPASP surface coatings was evaluated through analyses of WCA and functional density post-treatment with PBS, PPP, and ultrasound. Selected for this study were PASP, sPASP40, and sPASP80. Initially, these coatings were immersed in PBS (Fig. 5 A), which mimics physiological conditions. After a 14-day period, a noticeable decline in functional density was recorded for all samples: PASP to 66.3 $\pm$ 5.0%, sPASP40 to 52.4 $\pm$ 2.3%, and sPASP80 to 45.7 $\pm$ 4.6%. Correspondingly, the WCA of these surfaces increased, reaching values of 65.2 $\pm$ 1.6°, 58.8 $\pm$ 3.2°, and 66.7 $\pm$ 4.1°, respectively.

When subjected to immersion in PPP, a drastic reduction in functional density was observed for sPASP40 and sPASP80, plummeting to 28.9 $\pm$ 2.6% and 32.2 $\pm$ 4.3%, respectively, while PASP exhibited a

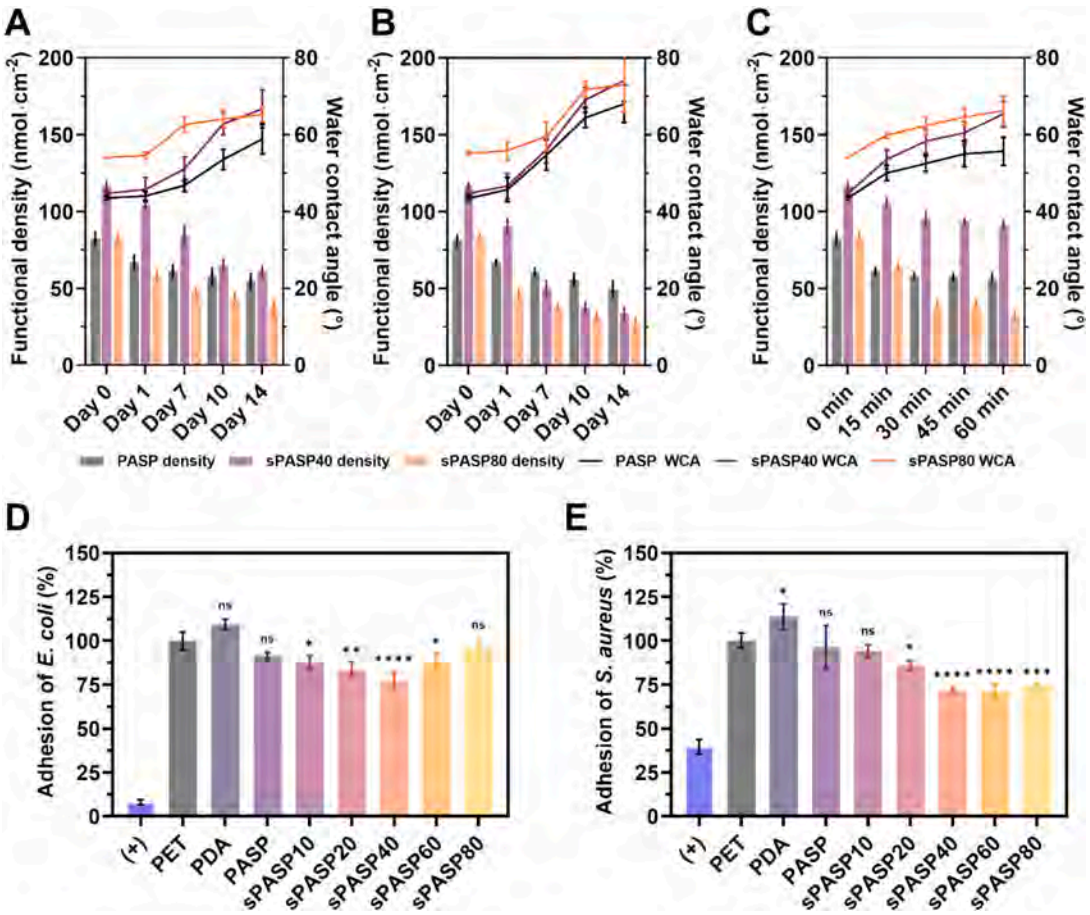

Fig. 5. Stability and antibacterial properties of sPASP coatings. Functional density and WCA of PASP, sPASP40, and sPASP80 in (A) PBS, (B) PPP, and (C) under sonication. Bacterial anti-adhesion performance of sPASP surfaces against (D) *E. coli* and (E) *S. aureus*.

marginal decrease to 61.2 ± 5.3%. The WCA of these surfaces also significantly increased compared to their response in PBS, indicative of the harsher conditions in the PPP environment, rich in proteins and enzymes (Fig. 5B), which may accelerate the decomposition of sPASP coatings. Notably, the durability of coatings like sPASP80 was adversely affected. As previously demonstrated, increasing the degree of sulfation resulted in a lower polymer coating density, which consequently led to reduced coating stability. Conversely, PASP showed better endurance due to its non-competitive reaction with AHS, allowing for a higher binding density with the PDA adhesive layer. In terms of WCA, sPASP40 and sPASP80, with higher sulfation levels, exhibited greater surface energy compared to PASP due to enhanced solvation of the sulfate groups. This is reflected in their maintained hydrophilicity despite a reduction in functional group density after 14 days.

The coating durability was further assessed under the influence of mechanical sound waves (Fig. 5C), revealing minimal impact on PASP and sPASP40, with functional group densities remaining substantial at 68.9 ± 3.0% and 78.0 ± 2.4%, respectively. In contrast, sPASP80 displayed less durability, with a functional group density of only 38.9 ± 0.5%, attributed to weaker bonding with the PDA layer. Similar trends were observed in WCA assessments for PASP, sPASP40, and sPASP80, with values of 66.2 ± 3.1°, 55.7 ± 3.0°, and 65.4 ± 2.7°, respectively. These findings support the hypothesis that densities of bonding between sPASP and PDA are influenced by the competitive conjugation with AHS sulfating moieties. Although higher sulfation levels may enhance anticoagulant properties, for the one-pot synthesis, sPASP40 emerges as the optimal variant in terms of overall properties. In summary, the 14-day biodegradation study ultimately showed that the coating retained its stability and integrity for only around seven days, after which a clear decline in durability was observed. This finding indicated that, for coatings prepared using sPASP, a short-term application would be more suitable than a long-term one in order to maintain the material's overall effectiveness.

3.8. Antibacterial adhesion of sPASP coatings

Additionally, the antibacterial properties of the sPASP coatings were evaluated, an essential aspect in biomimetic coatings for medical devices. *E. coli* and *S. aureus* anti-adhesion was tested using 0.01 mg·mL^{-1} kanamycin as a positive control, with PET serving as a baseline control. Coated surfaces were exposed to bacterial suspension, and bacterial viability was measured using alamarBlue reagent. It is noteworthy that the bacterial density used in this assessment was considerably higher than what is typically encountered in *in vivo* or clinical settings. Therefore, the findings presented below should be regarded as preliminary and supportive, rather than definitive in evaluating the antibacterial potential of sPASP as a coating for medical devices. According to Fig. 5D and E, PDA showed increased bacterial adhesion compared to PET, at 109.2 ± 2.5% for *E. coli* and 113.8 ± 5.8% for *S. aureus*, likely due to its positively charged functional groups enhancing bacterial cell membrane adhesion. Consistent with previous anti-biofouling studies, bacterial repulsion correlated with the SFE of each surface. sPASP40 demonstrated the lowest *E. coli* adhesion level at 76.9 ± 4.3%. Meanwhile, the sPASP60 sample exhibited the lowest *S. aureus* adhesion, recorded at 71.1 ± 3.2%, which was comparable to that of sPASP40 at 71.8 ± 1.3%, showing only a marginal difference between the two coatings. The primary antibacterial mechanism proposed in this study was attributed to electrostatic repulsion between the negatively charged

sPASP coatings and the phospholipid membranes of bacteria, combined with the repelling effect of the hydration layer formed by the hydrophilic polymer. Additionally, several other studies have suggested that sulfates may possess inherent antibacterial activity by disrupting bacterial membrane integrity through interactions with the sulfate groups [49,50]. These findings indicated that the sPASP coatings exhibited a degree of antibacterial or anti-adhesive activity, although its performance remained limited and would require further improvement. Therefore, incorporating additional surface modifications using antimicrobial drugs, antimicrobial peptides, or other antibacterial nanomaterials could further strengthen this property of the coating.

3.9. Antithrombogenicity of sPASP coatings under flow conditions

Following extensive analyses and optimisation efforts, Fig. S7 provides a comprehensive overview of all attributes of different sPASP variants, articulated through a heat map. This graphical representation highlights that, within the scope of one-pot synthesis methodology for sPASP coatings, sPASP40 emerges as the most effective variant, meeting a wide array of criteria in preliminary *in vitro* assessments. Consequently, sPASP40 has been selected as the representative formulation for subsequent research endeavors.

It is pertinent to note that medical devices in contact with blood are typically subjected to dynamic blood flow conditions. Under such circumstances, blood components exhibit heightened dynamism and a propensity for increased sensitivity to foreign materials. Factors such as shear stress and fluid dynamics critically influence cellular behaviour, rendering components like platelets more susceptible to reactivity. This increased reactivity amplifies the probability of interactions with foreign surfaces, potentially escalating risks of adhesion, activation, and thrombosis. Therefore, the assessment of biomaterials intended for use in blood-contacting devices necessitates a thorough understanding of these flow-induced sensitivities.

In light of these considerations, the performance of sPASP coatings was scrutinised using two prevalent *in vitro* models: Chandler loop and microfluidic device, as demonstrated in Fig. 6A and B. The findings, illustrated in Fig. 6C—H, reveal notable alterations in haemofactors post-experiment. Specifically, by assessing the whole blood after being perfused through the coated channels, a modest reduction in the three primary blood cell types (RBCs, platelets, leukocytes) was observed in comparison with the original figures in the control non-perfused blood, yet the counts remained substantially higher than in non-coated models, particularly for platelets and leukocytes. Under flow conditions, these cells exhibit increased sensitivity, likely adhering to the walls of the flow models, which could precipitate surface-induced thrombosis and inflammatory reactions. Furthermore, assessments of haemoglobin levels and erythrocyte lysis rates indicated that sPASP40-coated samples offer enhanced blood compatibility, reducing the likelihood of surface-induced erythrocyte degradation. The anti-platelet adhesion capabilities were further substantiated using microfluidic devices with DiOC6-stained platelets. Uncoated surfaces exhibited significant platelet adherence, whereas sPASP40-coated surfaces showed minimal platelet attachment, as shown in Fig. 6I and J. In addition, the HEP sample used for comparison with sPASP in the microfluidic model after 3 h produced a similarly low signal (Fig. S8), with a value of 9.2 ± 0.6 RFU $\times 10^4$. This outcome suggested that sPASP exhibited a comparable potential to HEP in resisting platelet adhesion and supporting anticoagulant performance. This substantiates the potential use of sPASP coatings for biological applications, underscoring their efficacy in preventing surface-induced coagulation both *in vitro* and potentially *in vivo*.

3.10. In vivo inflammatory response

Following subcutaneous implantation of both coated and uncoated surfaces, murine skin tissues were harvested for histological evaluation to assess inflammation associated with the presence of the implanted materials (Fig. 7A). Overall, the suture site on the mice remained stable after 7 days and exhibited no signs of abnormalities or inflammation, as illustrated in Fig. 7B. As shown in Fig. 7C, tissue surrounding the implanted surfaces exhibited fibrous encapsulation. Notably, this capsule layer appeared substantially thicker around plain PET surfaces in comparison with those coated with sPASP. The formation of such fibrotic tissue is understood to act as a defensive mechanism against foreign bodies, whereby increased capsule thickness typically reflects a more pronounced inflammatory response and subsequent collagen fibre deposition to isolate incompatible materials from host tissues [3].

Representative histological images stained with H&E are presented in Fig. 7D, while the corresponding quantitative analysis of capsule thickness is shown in Fig. 7F. In the uncoated PET group, capsule thickness increased markedly and was consistent with macroscopic observations. By contrast, the sPASP-coated surfaces exhibited a marginal increase in capsule thickness (11.7 ± 3.1 μm), which was statistically indistinguishable from that observed in healthy skin (11.3 ± 3.6 μm), suggesting minimal inflammatory encapsulation.

Furthermore, inflammatory cell density was substantially elevated in the PET-implanted tissues. High-magnification images (20×) revealed dense infiltration of inflammatory cells at the implant–tissue interface, with a leukocyte density of 121.9 ± 38.2 cells·mm^{-2}, as depicted in Fig. 7G. In contrast, the sPASP-coated group demonstrated significantly lower leukocyte infiltration (23.9 ± 11.1 cells·mm^{-2}), with no statistically significant difference from the healthy control. These findings were summarised in the inflammatory reaction score (Fig. 7H), confirming a heightened inflammatory profile in PET surfaces due to increased immune cell migration and infiltration, whereas sPASP coatings elicited only a modest immune response.

The biocompatibility of the materials was further supported by the immunohistochemical evaluation of CD163, a well-established marker of M2-polarised macrophages, indicative of anti-inflammatory and pro-regenerative activity. As shown in Fig. 7E, CD163-positive cells (red fluorescence) were virtually absent in tissues surrounding the uncoated PET implants. Conversely, sPASP-coated surfaces exhibited clear M2 polarisation as early as day 7 post-implantation, especially in regions beneath the fibrous capsule and along the smooth muscle layer stained with α-SMA (green fluorescence). Quantitative FI measurements of CD163 (Fig. 7I) confirmed this trend, with sPASP samples reaching 1255 ± 450.6 RFU, significantly higher than the PET group (575.2 ± 254.5 RFU) and the untreated control. Collectively, these findings corroborate the *in vivo* biocompatibility of the sPASP coating. The demonstrated attenuation of localised inflammation and promotion of a regenerative immune profile underscore the suitability of this material for biomedical applications, particularly for surface coatings in blood-contacting devices, where suppression of immune-triggered coagulation is crucial.

4. Conclusion

This study was based on the hypothesis that the introduction of sulfate groups into poly(aspartic acid) (PASP) would enhance anticoagulant and antibacterial properties at the material–blood interface, thus addressing key limitations of blood-contacting medical devices. The research aimed to develop a biomimetic coating through a one-pot modification strategy, using PASP as a biodegradable backbone, to achieve a multifunctional material capable of reducing thrombosis, microbial adhesion, and inflammation. Among the different variants, the sPASP40 formulation, incorporating 40% sulfation, emerged as the most outstanding, demonstrating a superior balance between coating stability and biological activity. Specifically, sPASP40 coatings exhibited significantly enhanced haemocompatibility, as evidenced by the reduction in non-specific protein adsorption, decreased platelet adhesion both in static and dynamic flow models, and marked prolongation of APTT and TT. Moreover, thrombin generation assays confirmed the effective suppression of thrombin activity, validating the anticoagulant performance of the material. Importantly, sPASP coatings induced

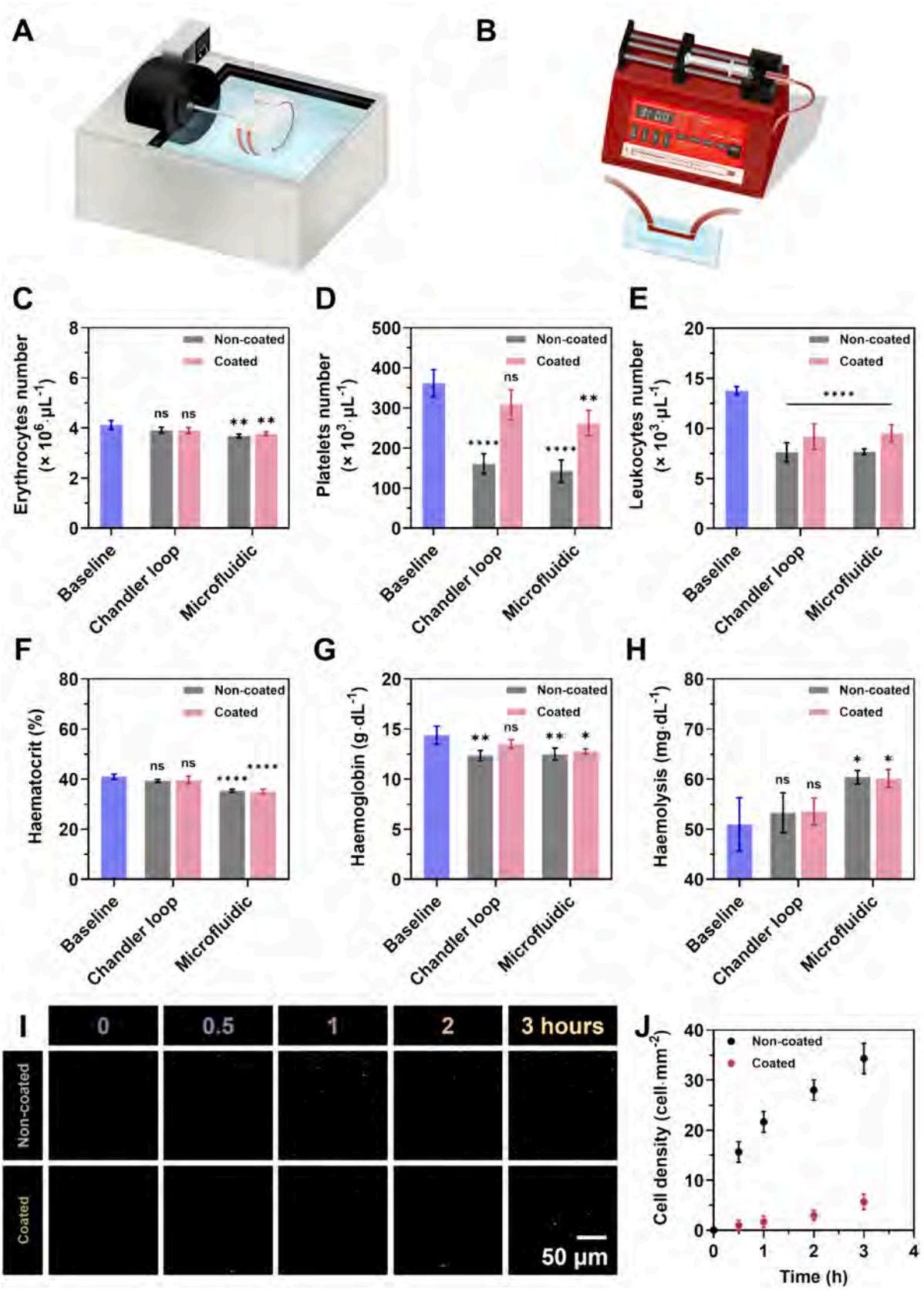

Fig. 6. *In vitro* antithrombogenic assessment under flow using (A) Chandler loop and (B) microfluidic device models. Analyses six haemofactors pre- and post-operation: (C) erythrocyte, (D) platelet, (E) leukocyte counts; (F) haematocrit; (G) haemoglobin; (H) haemolysis. (I) Representative images of DiOC6-stained platelet binding on sPASP-coated and non-coated microfluidic devices, illustrating antiplatelet effects and (J) platelet density counted accordingly.

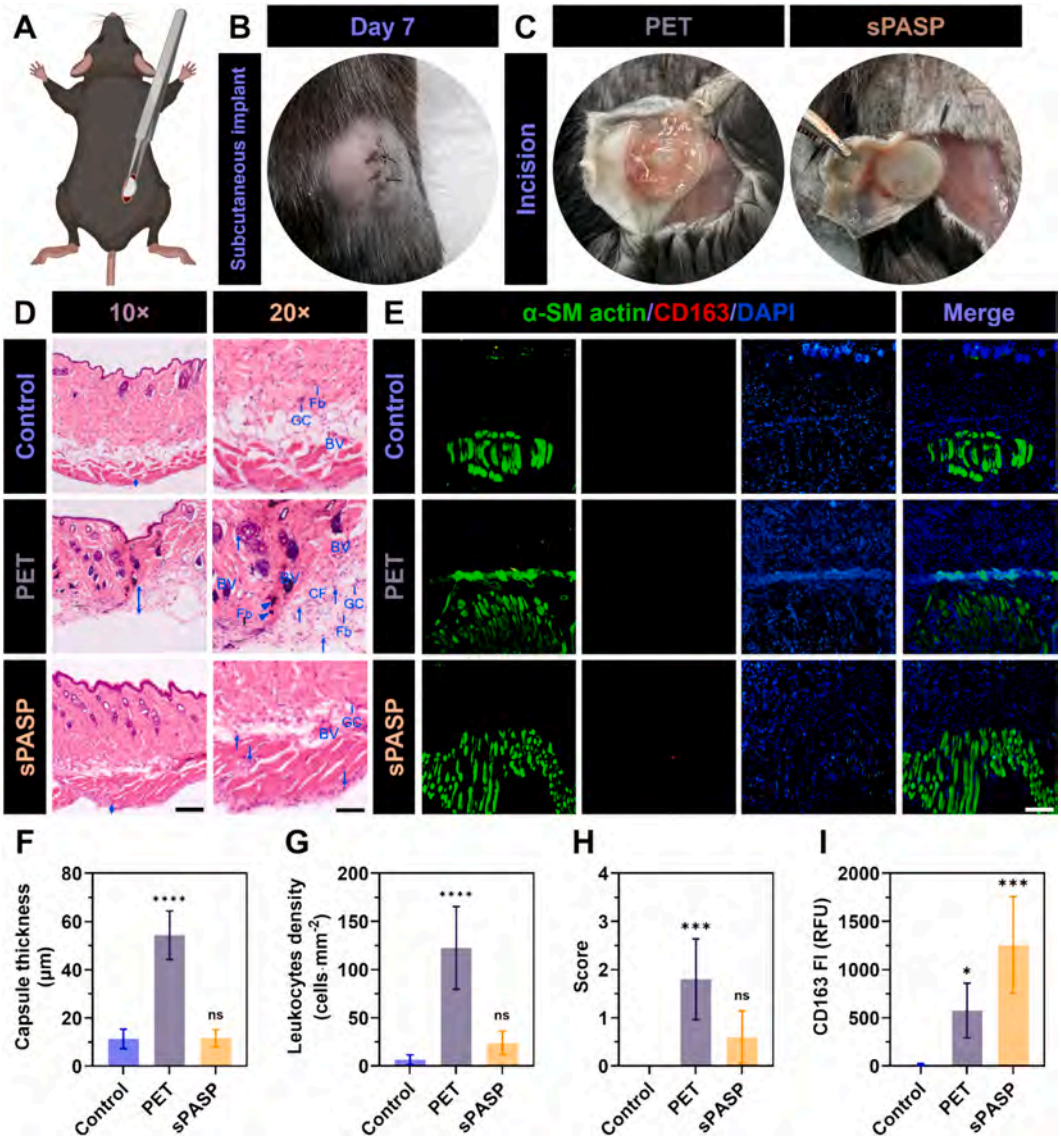

Fig. 7. Evaluation of the inflammatory response induced by subcutaneously implanted surface coatings in mice. (A) Illustration of subcutaneous implantation in the C57BL/6 mice model. Created in BioRender. Luu, C. (2025) https://BioRender.com/dcsoumi. (B) Suture site at the implantation site after 7 days. (C) Images of explanted plain PET and sPASP-coated samples following surgical retrieval. (D) Representative H&E-stained tissue images captured at 10× and 20× magnifications. Scale bars represent 200 μm and 100 μm, respectively. Observations included the presence of capsule layers (two-way arrows), inflammatory cells (one-way arrows), necrotic cells (triangular pointer), fibroblasts (Fb), multinucleated giant cells (GC), collagen fibres (CF), and blood vessels (BV). (E) Immunohistochemical staining results using α-SMA (green) and CD163 (blue) antibodies, counterstained with DAPI. Quantitative evaluations of (F) capsule thickness, (G) leukocyte density, (H) inflammation score, and (I) CD163 FI were obtained from stained tissue samples.

minimal immune activation, with low haemolysis rates, reduced ROS production in macrophages, and favourable cytocompatibility towards both endothelial cells and macrophages. These results were further corroborated *in vivo*, where sPASP40 coatings elicited minimal inflammatory responses following subcutaneous implantation, as demonstrated by reduced capsule thickness, lower leukocyte density, and a shift towards M2 macrophage polarisation. In addition to its haemocompatibility, sPASP40 also demonstrated moderate antibacterial properties against *E. coli* and *S. aureus* adhesion and satisfactory chemical and mechanical durability in PBS, blood plasma, and under ultrasonic conditions. The results clearly indicate that sPASP holds comparable potential to other coating materials based on heparin or heparin-mimicking polysaccharides. The data consistently highlighted enhanced blood compatibility and overall surface functionality, indicating that sPASP holds a notable advantage over conventional polysaccharide-based coatings across multiple evaluation parameters. These findings strongly support the overall success of the research hypothesis and objectives, establishing sPASP40 as a highly promising candidate for future biomedical coatings intended for blood-contacting devices.

However, some limitations must be acknowledged. While the antibiofouling and anticoagulant properties were well demonstrated *in vitro* and in preliminary *in vivo* settings, the antimicrobial efficacy remained moderate, necessitating further enhancements to meet clinical demands. Additionally, long-term *in vivo* studies, particularly in blood-contacting environments such as vascular implants, are required to fully validate the functionality and durability of the coatings under physiological conditions. Future directions should focus on optimising the antimicrobial properties of sPASP by integrating complementary strategies, such as incorporating antimicrobial peptides or nitric oxide donors, without compromising its haemocompatibility. Besides, a more detailed comparison between the coating performance of sPASP and

heparan sulfate should be further elaborated to better illustrate the potential of sPASP as a viable alternative. Furthermore, tailoring the sulfation pattern along the PASP backbone, mimicking natural heparin more precisely, may yield a comparable anticoagulant activity and improved biostability. Scaling up the production and evaluating device-specific applications, such as vascular grafts and catheters, would be critical to advancing the translational potential of this promising material.

CRediT authorship contribution statement

Cuong Hung Luu: Writing – original draft, Visualization, Methodology, Investigation, Formal analysis, Conceptualization. **Akriti Nepal:** Investigation. **Nam-Trung Nguyen:** Writing – review & editing, Supervision. **Hang Thu Ta:** Writing – review & editing, Supervision, Resources, Project administration, Funding acquisition, Conceptualization.

Declaration of competing interest

The authors declare the following financial interests/personal relationships which may be considered as potential competing interests: Hang Thu Ta reports financial support was provided by National Health and Medical Research Council. Hang Thu Ta reports financial support was provided by National Heart Foundation of Australia. Hang Thu Ta reports financial support was provided by Australian Research Council. If there are other authors, they declare that they have no known competing financial interests or personal relationships that could have appeared to influence the work reported in this paper.

Acknowledgement

This work and H.T.T are supported by the National Health and Medical Research Council (APP1182347, and APP2002827 to H.T.T.), National Heart Foundation of Australia (102761 to H.T.T.), Australian Research Council (FT240100280 to H.T.T). C.H.L and A.N are supported by Griffith University PhD scholarships. It is also supported by Griffith University and the University of Queensland Australian National Fabrication Facilities (ANFF).

Appendix A. Supplementary data

Supplementary data to this article can be found online at https://doi.org/10.1016/j.bioadv.2026.214723.

Data availability

Data will be made available on request.

References

[1] C.H. Luu, N.-T. Nguyen, H.T. Ta, Unravelling surface modification strategies for preventing medical device-induced thrombosis, Adv. Healthc. Mater. 13 (1) (2024) 2301039.
[2] D.L. Tran, et al., Multifunctional surfaces through synergistic effects of heparin and nitric oxide release for a highly efficient treatment of blood-contacting devices, J. Control. Release 329 (2021) 401–412.
[3] M. Yao, et al., A starch-based zwitterionic hydrogel coating for blood-contacting devices with durability and bio-functionality, Chem. Eng. J. 421 (2021) 129702.
[4] R. Gbyli, et al., Achieving totally local anticoagulation on blood contacting devices, Adv. Mater. Interfaces 5 (4) (2018) 1700954.
[5] J.T. Wolfe, A. Shradhanjali, B.J. Tefft, Strategies for improving endothelial cell adhesion to blood-contacting medical devices, Tissue Eng. Part B Rev. 28 (5) (2022) 1067–1092.
[6] P.-K.T. Ngo, et al., Multifunctional haemostatic and antibacterial wound dressing: chitosan-silk fibroin composite with green-synthesised silver nanoparticles and deferoxamine, Surf. Interfaces 72 (2025) 107112.
[7] R. Biran, D. Pond, Heparin coatings for improving blood compatibility of medical devices, Adv. Drug Deliv. Rev. 112 (2017) 12–23.
[8] N.T.T. Le, et al., The physicochemical and antifungal properties of eco-friendly silver nanoparticles synthesized by Psidium guajava leaf extract in the comparison with Tamarindus indica, J. Clust. Sci. 32 (3) (2021) 601–611.
[9] K.X. Vazquez-Prada, et al., A spiky silver-Iron oxide nanoparticle for highly efficient targeted photothermal therapy and multimodal imaging of thrombosis, Small 19 (11) (2023) 2205744.
[10] M. Cloutier, D. Mantovani, F. Rosei, Antibacterial coatings: challenges, perspectives, and opportunities, Trends Biotechnol. 33 (11) (2015) 637–652.
[11] S. Gao, et al., Dressing antibacterial platinum loaded polyurethane materials by a stable hydrophilic coating with robust antithrombotic properties, Biomed. Mater. 20 (3) (2025) 035035.
[12] V.H.G. Phan, et al., Longan-inspired chitosan-pectin core-shell hydrogel beads for oral delivery of biodrugs to enhance osteoporosis therapy, Int. J. Biol. Macromol. 308 (2025) 142254.
[13] C.M. Phan, et al., Injectable gelatin-pectin hydrogel for dental tissue engineering: enhanced angiogenesis and antibacterial efficacy for pulpitis therapy, Int. J. Biol. Macromol. 284 (2025) 137939.
[14] N.-Q.T. Nguyen, et al., Dual-functional injectable hydrogels as antimicrobial and angiogenic therapeutics for dental pulp regeneration, J. Mater. Chem. B 13 (23) (2025) 6765–6783.
[15] W. Khan, S. Farah, A.J. Domb, Drug eluting stents: developments and current status, J. Control. Release 161 (2) (2012) 703–712.
[16] D. Fan, X. Liu, H. Chen, Endothelium-mimicking materials: a “rising star” for antithrombosis, ACS Appl. Mater. Interfaces 16 (40) (2024) 53343–53371.
[17] L. Huang, et al., Sulfated polysaccharides: immunomodulation and signaling mechanisms, Trends Food Sci. Technol. 92 (2019) 1–11.
[18] J.B.M. Rocha Neto, et al., Polysaccharide-based layer-by-layer nanoarchitectonics with sulfated chitosan for tuning anti-thrombogenic properties, Colloids Surf. B: Biointerfaces 213 (2022) 112359.
[19] L. Ma, et al., Anticoagulant sodium alginate sulfates and their mussel-inspired heparin-mimetic coatings, J. Mater. Chem. B 4 (19) (2016) 3203–3215.
[20] S. Palanisamy, et al., In vitro antioxidant and antibacterial activity of sulfated polysaccharides isolated from Spatoglossum asperum, Carbohydr. Polym. 170 (2017) 296–304.
[21] S.J. Paluck, T.H. Nguyen, H.D. Maynard, Heparin-mimicking polymers: synthesis and biological applications, Biomacromolecules 17 (11) (2016) 3417–3440.
[22] S. Yao, et al., Anti-fouling coatings for blood-contacting devices, Smart Mater. Med. 5 (1) (2024) 166–180.
[23] J. Hu, et al., Recent progress in antibacterial surfaces for implant catheters, BME Front. 6 (2025) 0063.
[24] W. Li, et al., Host-defense-peptide-mimicking β-peptide polymer acting as a dual-modal antibacterial agent by interfering quorum sensing and killing individual bacteria simultaneously, Research 6 (2023) 0051.
[25] Q. Ma, et al., Bioinspired zwitterionic block polymer-armored nitric oxide-generating coating combats thrombosis and biofouling, Research 7 (2024) 0423.
[26] H. Adelnia, et al., Poly(succinimide) nanoparticles as reservoirs for spontaneous and sustained synthesis of poly(aspartic acid) under physiological conditions: potential for vascular calcification therapy and oral drug delivery, J. Mater. Chem. B 11 (12) (2023) 2650–2662.
[27] H. Adelnia, et al., A bioactive disintegrable polymer nanoparticle for synergistic vascular anticalcification, ACS Nano 17 (19) (2023) 18775–18791.
[28] H. Adelnia, et al., Metal ion chelation of poly(aspartic acid): from scale inhibition to therapeutic potentials, Int. J. Biol. Macromol. 229 (2023) 974–993.
[29] H. Adelnia, et al., Poly(aspartic acid) in biomedical applications: from polymerization, modification, properties, degradation, and biocompatibility to applications, ACS Biomater Sci. Eng. 7 (6) (2021) 2083–2105.
[30] Y. Liu, et al., Anticoagulant dialyzer with enhanced Ca2+ chelation and hydrophilicity for heparin free hemodialysis, J. Membr. Sci. 604 (2020) 118082.
[31] G. Lima-Oliveira, et al., Clot activators and anticoagulant additives for blood collection. A critical review on behalf of COLABIOCLI WG-PRE-LATAM, Crit. Rev. Clin. Lab. Sci. 58 (3) (2021) 207–224.
[32] H.H. Vu, et al., Tunable wettability with stretchable microstructured surfaces, Adv. Eng. Mater. 25 (23) (2023) 2300821.
[33] P. Soman, C.A. Siedlecki, Effects of protein solution composition on the time-dependent functional activity of fibrinogen on surfaces, Langmuir 27 (17) (2011) 10814–10819.
[34] T.-H.H. Tran, et al., Mineralized biopolymers-based scaffold encapsulating with dual drugs for alveolar ridge preservation, Macromol. Biosci. 25 (2) (2025) 2400351.
[35] N.H.T. Luu, et al., Cholesterol-conjugated PAMAM dendrimers: enhancing stability, drug delivery efficiency, and in vitro anticancer performance, J. Polym. Sci. 63 (3) (2025) 541–553.
[36] V. Sovkova, et al., Cellular response to individual components of the platelet concentrate, Int. J. Mol. Sci. 22 (9) (2021) 4539.
[37] F. Depasse, et al., Thrombin generation assays are versatile tools in blood coagulation analysis: a review of technical features, and applications from research to laboratory routine, J. Thromb. Haemost. 19 (12) (2021) 2907–2917.
[38] L. Sandrini, et al., Impact of acute and chronic stress on thrombosis in healthy individuals and cardiovascular disease patients, Int. J. Mol. Sci. 21 (21) (2020) 7818.
[39] M.M. Delfino, et al., Immunoinflammatory response and bioactive potential of GuttaFlow bioseal and MTA Fillapex in the rat subcutaneous tissue, Sci. Rep. 10 (1) (2020) 7173.
[40] B. Neri, et al., Histological scores in inflammatory bowel disease, J. Dig. Dis. 22 (1) (2021) 9–22.
[41] H. He, et al., Preparation and properties of a hyperbranch-structured polyamine adsorbent for carbon dioxide capture, Sci. Rep. 7 (1) (2017) 3913.
[42] M. Murugesan, et al., Tailoring hyaluronic acid hydrogels: impact of cross-linker length and density on skin rejuvenation as injectable dermal fillers and their

potential effects on the MAPK signaling pathway suppression, Bioact. Mater. 49 (2025) 154–171.
[43] L.R. Bush, D. Patrick, The role of the endothelium in arterial thrombosis and the influence of antithrombotic therapy, Drug Dev. Res. 7 (4) (1986) 319–340.
[44] Y. Li, et al., Integrated and hyaluronic acid-coated mesoporous silica nanoparticles conjugated with cisplatin and chlorin e6 for combined chemo and photodynamic cancer therapy, Eur. Polym. J. 220 (2024) 113426.
[45] P.-K.T. Ngo, et al., Silk fibroin/chitosan/montmorillonite sponge dressing: enhancing hemostasis, antimicrobial activity, and angiogenesis for advanced wound healing applications, Int. J. Biol. Macromol. 279 (2024) 135329.
[46] H.D.N. Tran, et al., Influence of nanoparticles on the haemostatic balance: between thrombosis and haemorrhage, Biomater. Sci. 10 (1) (2022) 10–50.
[47] S. Kim, et al., A biostable, anti-fouling zwitterionic polyurethane-urea based on PDMS for use in blood-contacting medical devices, J. Mater. Chem. B 8 (36) (2020) 8305–8314.
[48] M.C.L. Martins, et al., Albumin and fibrinogen adsorption on PU–PHEMA surfaces, Biomaterials 24 (12) (2003) 2067–2076.
[49] H. Ruan, et al., Polysaccharide-based antibacterial coating technologies, Acta Biomater. 168 (2023) 42–77.
[50] J.-Y. Jun, et al., Antimicrobial and antibiofilm activities of sulfated polysaccharides from marine algae against dental plaque bacteria, Mar. Drugs 16 (9) (2018) 301.

SUPPLEMENTARY INFORMATION

Sulfated Poly(Aspartic Acid) Coatings as Next-Generation Biomimetic Interfaces for Blood-Contacting Devices

Cuong Hung Luu [1], Akriti Nepal [1], Nam-Trung Nguyen [2,3], Hang Thu Ta [1,2,*]

[1] *School of Environment and Science, Griffith University, Nathan, QLD 4111, Australia*

[2] *Queensland Quantum and Advanced Technologies Research Institute, Griffith University, Nathan, QLD 4111, Australia*

[3] *School of Engineering and Built Environment, Griffith University, Nathan, QLD 4111, Australia*

[*] *Corresponding authors:*

***Hang Thu Ta**, BEng, MSc, PhD*

***Professor**, School of Environment and Science, and Queensland Micro- and Nanotechnology, Griffith University, Nathan Campus, Brisbane QLD 4111, Australia*

Australian Research Council Future Fellow

Australian Heart Foundation Future Leader Fellow

Office: +61 (7) 3735 5384

Email: h.ta@griffith.edu.au

Website: https://hangta.group/

https://experts.griffith.edu.au/27034-hang-ta

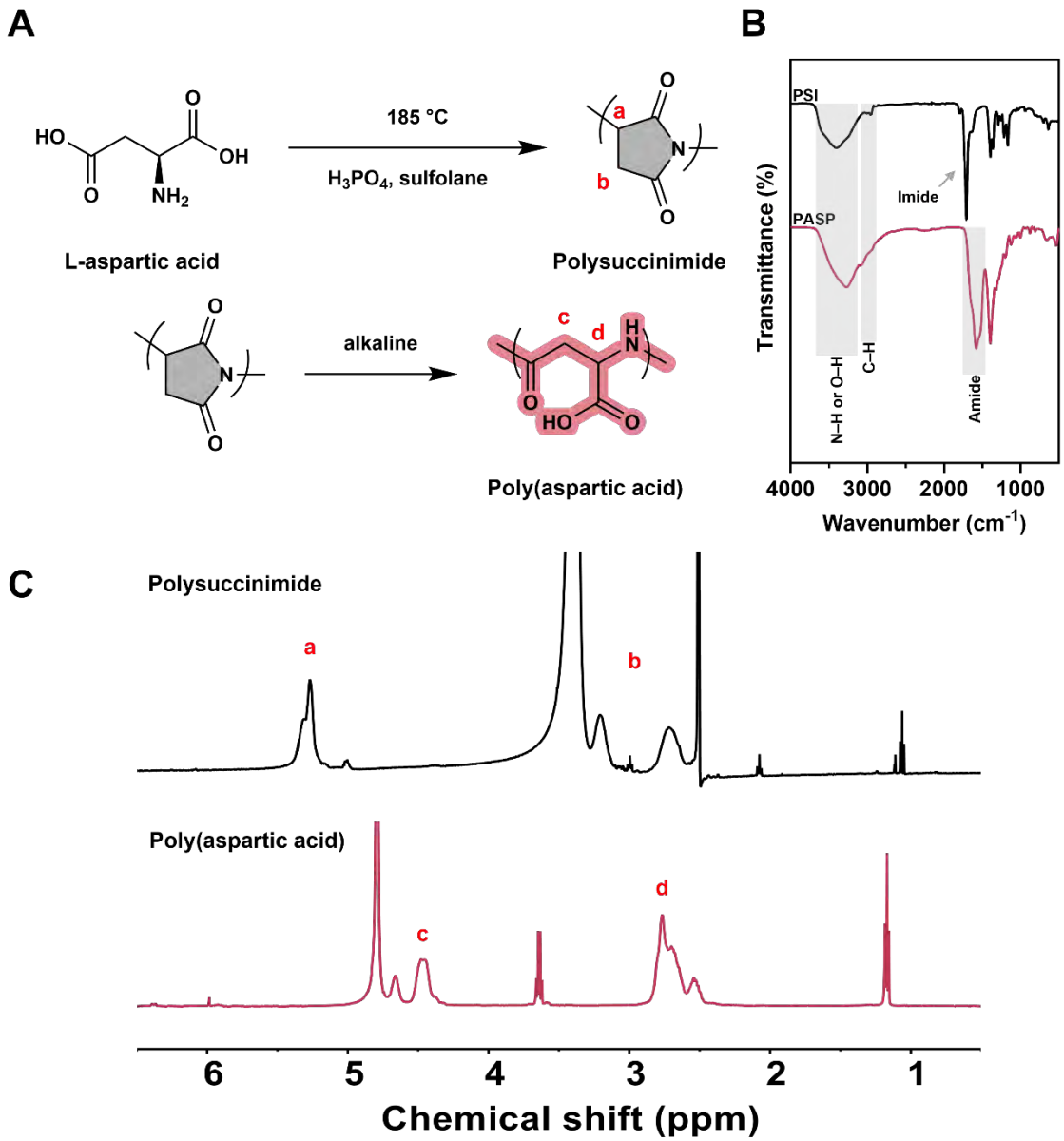

Figure S1. Synthesis and characterisation of PSI and PASP polymers. **(A)** Overall reactions involved in PSI and PASP syntheses. **(B)** ATR-FTIR spectra of PSI and PASP. **(C)** ^{1}H NMR spectra of PSI and PASP.

Table S1. Concentrations of reactants in sPASP coatings fabrication

	PASP	sPASP10	sPASP20	sPASP40	sPASP60	sPASP80	HEP
PASP (mg·mL^{-1})	2.0	2.0	2.0	2.0	2.0	2.0	2.0*
EDC (mM)	6.3	8.3	10.4	14.6	18.8	22.9	14.6
AHS (mM)	0.0	1.7	3.5	7.0	10.4	13.9	0.0

*Heparin was used instead of PASP.

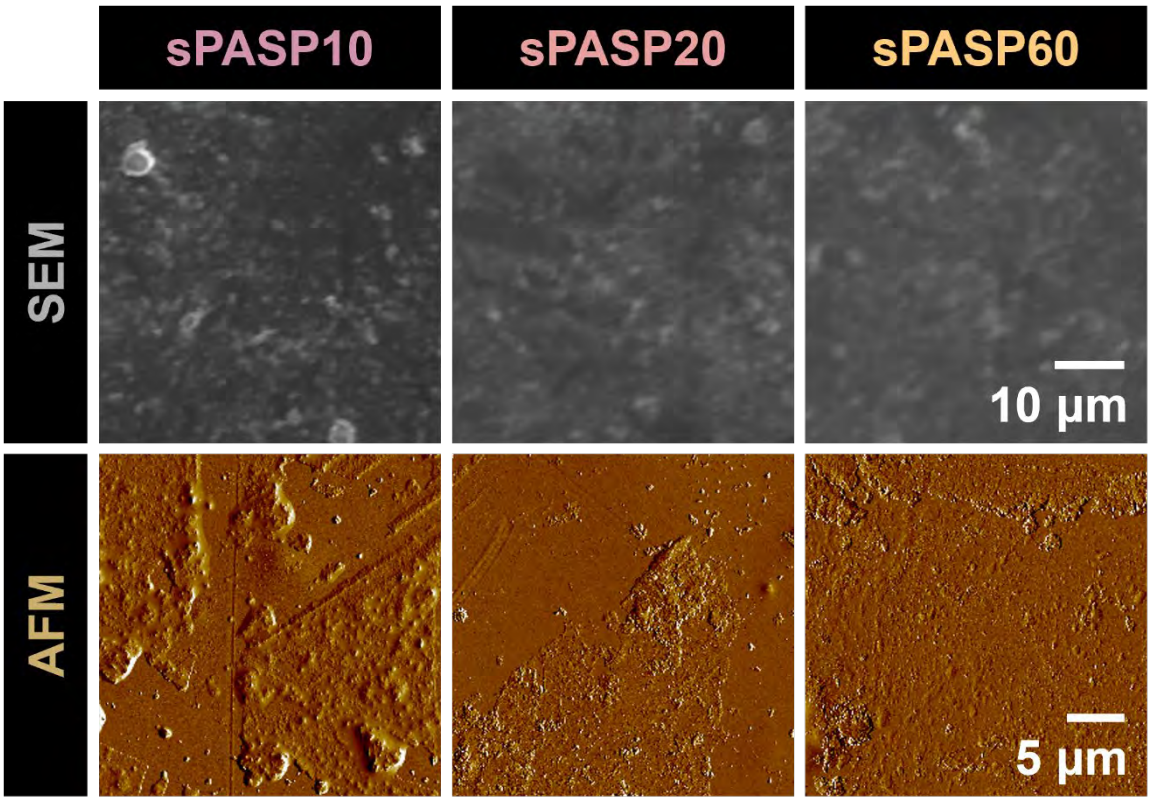

Figure S2. SEM and AFM images of sPASP10, sPASP20, sPASP60.

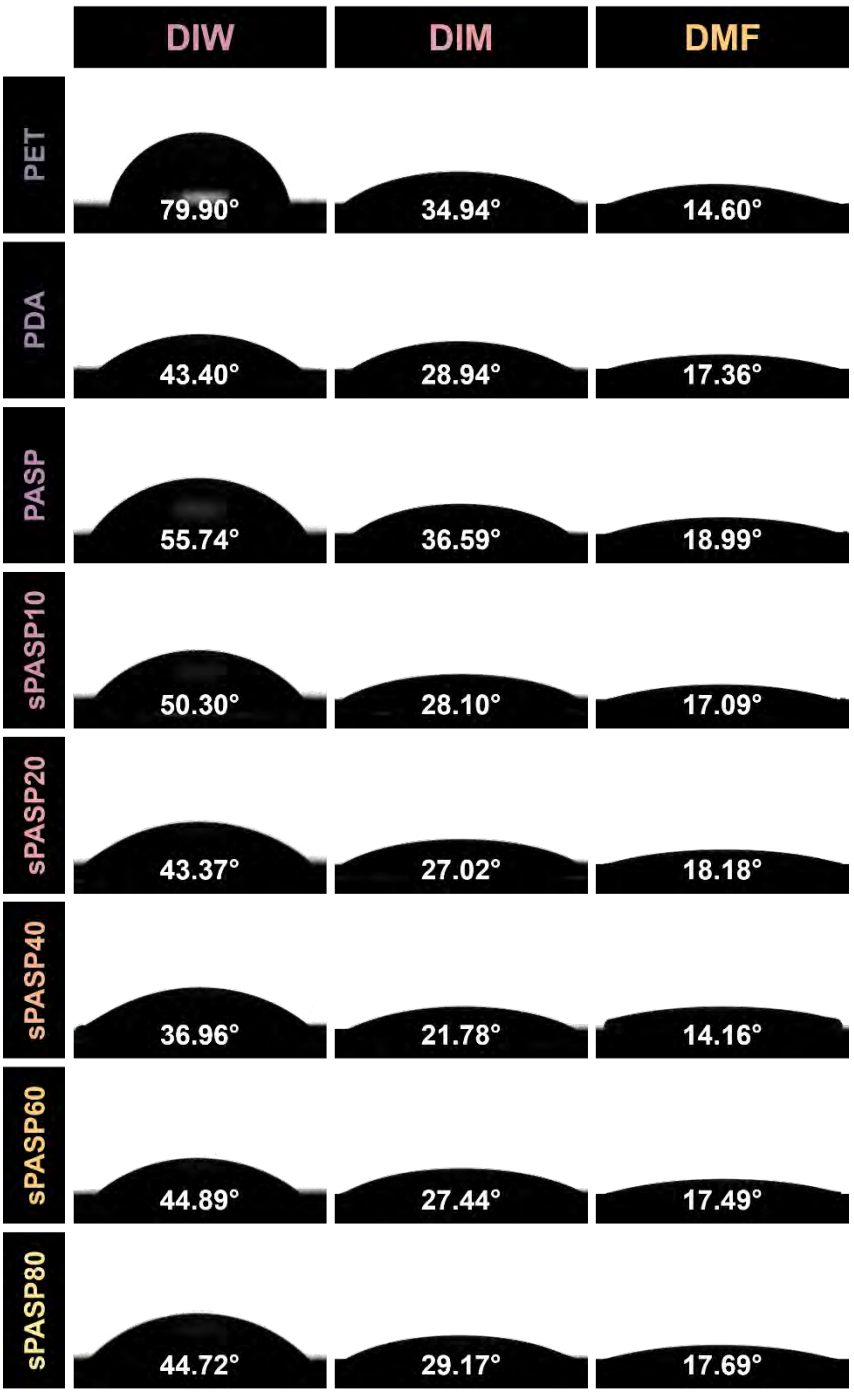

Figure S3. Contact angle measurements of plain PET, PDA, sPASP coatings with water, DIM, DMF, captured by a contact angle system (Attension® Theta Flex, Biolin Scientific AB, Sweden).

Table S2. Assessment of contact angle and liquid surface tension across all surfaces. The SFE for each surface was calculated utilising the Fowkes theory, also referred to as the Owens-Wendt-Rabel-Kaelble (OWRK) model. This calculation was based on contact angle measurements with water and DIM. The precision of these calculations was audited by deriving the coefficient of determination (R^2) from the regression line, which was aligned with the contact angle measurements using DMF

	Contact angle (°)			Surface energy (mN·m⁻¹)			R^2
	H_2O	DIM	DMF	γ^d_S	γ^p_S	SFE	
PET	79.90 ± 0.15	34.94 ± 0.52	14.60 ± 0.12	0.49 ± 0.60	14.38 ± 2.85	14.87 ± 3.45	0.9928 ± 0.0059
PDA	43.40 ± 0.44	28.94 ± 0.29	17.36 ± 0.28	2.32 ± 1.47	43.51 ± 0.93	45.83 ± 2.23	0.9871 ± 0.0047
PASP	55.74 ± 0.06	36.59 ± 0.12	18.99 ± 0.08	15.67 ± 3.32	36.80 ± 3.03	52.47 ± 2.20	0.9946 ± 0.0033
sPASP10	50.30 ± 0.67	28.10 ± 0.44	17.09 ± 0.10	4.15 ± 0.37	56.04 ± 1.82	60.20 ± 2.00	0.9930 ± 0.0057
sPASP20	43.37 ± 0.22	27.02 ± 0.52	18.18 ± 0.41	4.78 ± 0.34	58.52 ± 2.61	63.30 ± 2.89	0.9965 ± 0.0018
sPASP40	36.96 ± 0.71	21.78 ± 0.26	14.16 ± 0.23	3.74 ± 0.75	62.82 ± 1.44	66.57 ± 1.02	0.9925 ± 0.0088
sPASP60	44.89 ± 0.29	27.44 ± 0.63	17.49 ± 0.37	4.72 ± 1.96	47.33 ± 2.02	52.05 ± 0.83	0.9954 ± 0.0058
sPASP80	44.72 ± 0.35	29.17 ± 0.58	17.69 ± 0.69	4.94 ± 1.82	44.76 ± 2.82	49.70 ± 2.36	0.9948 ± 0.0031

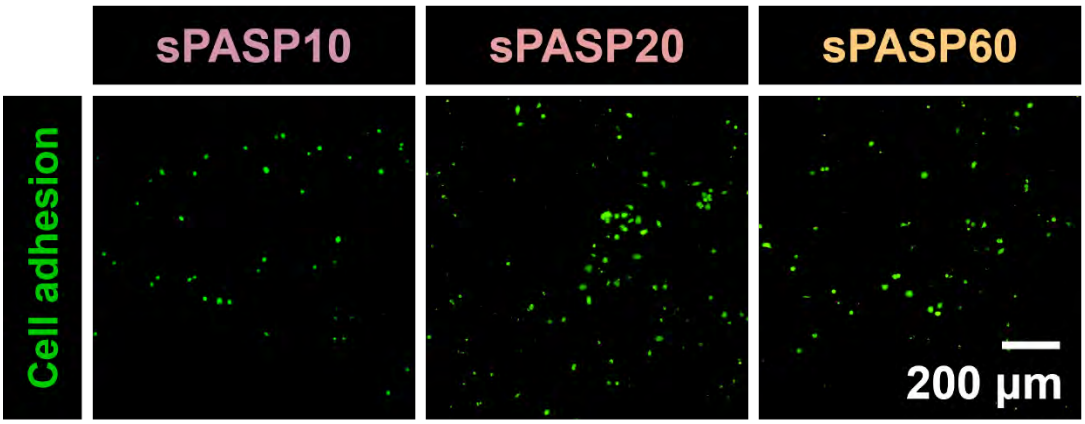

Figure S4. Fluorescence microscopic images of SVEC4-10 cell adhesion on sPASP10, sPASP20, and sPASP60 surface coatings. The cells were visualised following staining with fluorescent dyes.

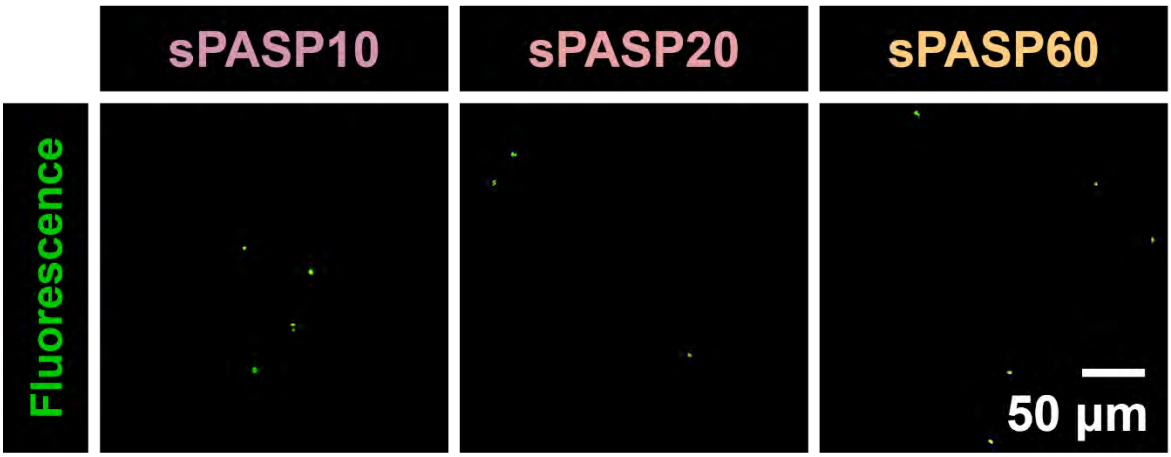

Figure S5. Visualisation of platelet adhesion on sPASP10, sPASP20, and sPASP60 surfaces using fluorescence microscopy.

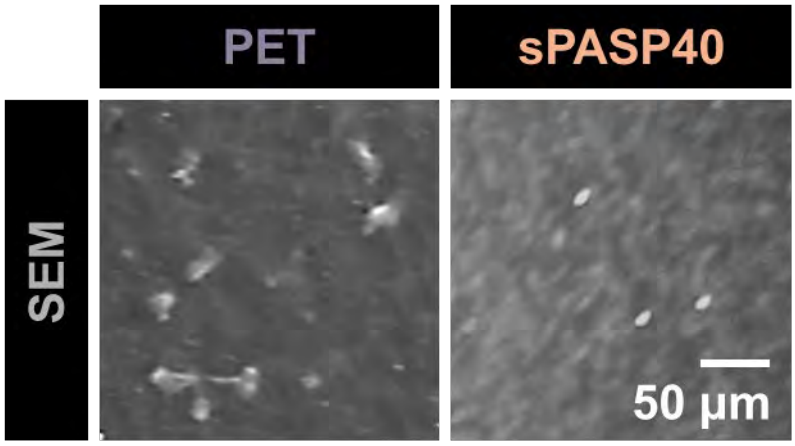

Figure S6. Platelet adhesion on PET and sPASP40 samples observed by SEM.

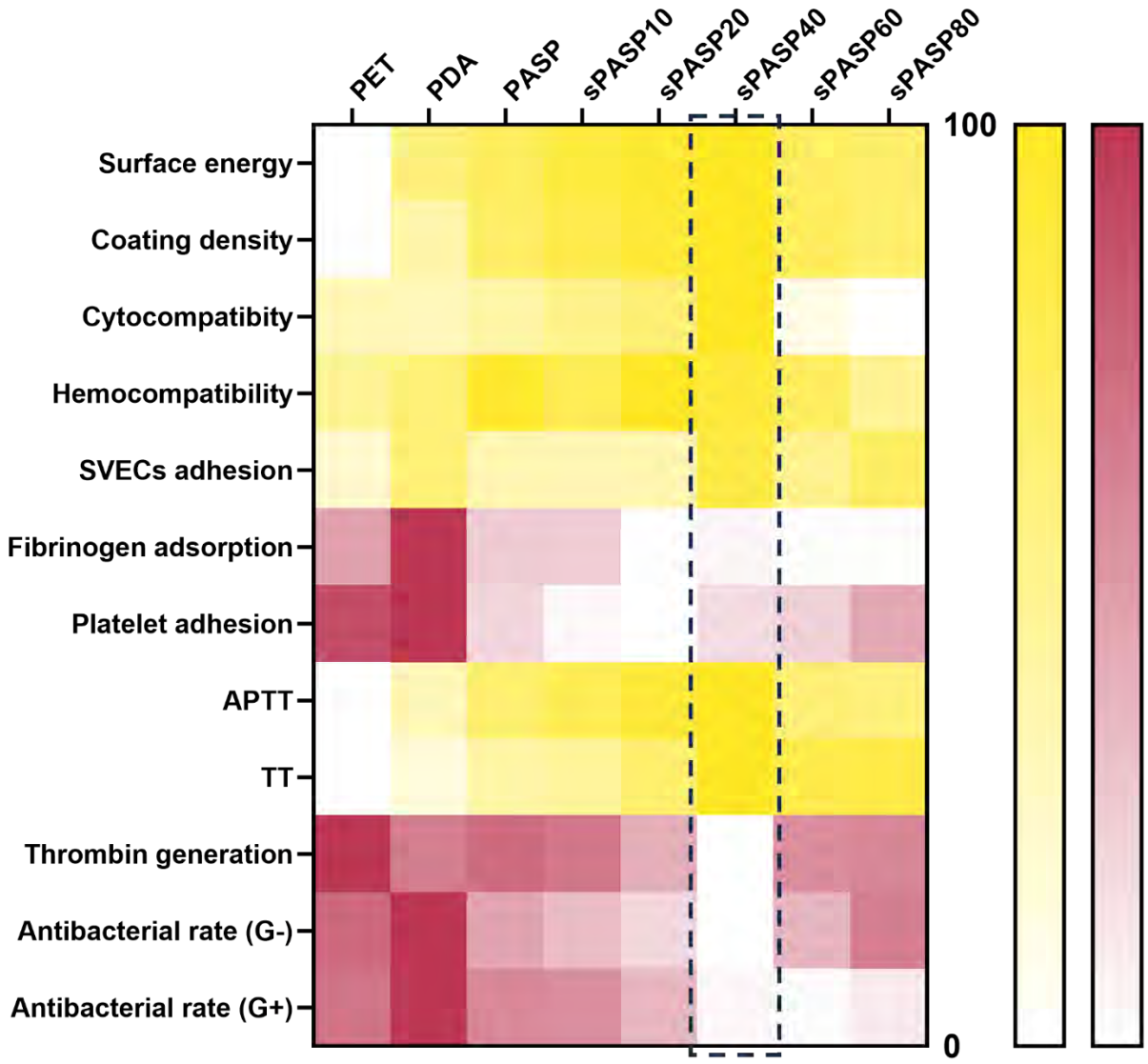

Figure S7. Summary of optimised results through surface property evaluations related to potential antithrombosis and antibacterial performance.

Table S3. Setup paramaters used for antithrombosis evaluations under dynamic flow conditions for both Chandler loop and microfluidic device models.

	Chandler loop	**Microfluidic device**
Inner diameter	5 mm	–
Length	50 cm	20 mm
Flow rate	30 rpm	31 $\mu L \cdot min^{-1}$
Shear rate	~500 s^{-1}	1000 s^{-1}
Duration time	3 h	3 h

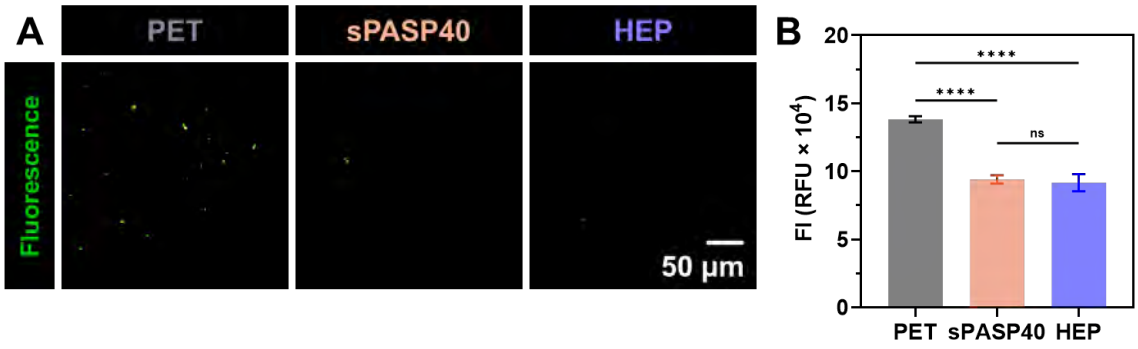

Figure S8. Comparison of platelet resistance on microfluidic devices between PET, sPASP40, and HEP. **(A)** Stained images of platelets adhered to the respective surfaces. **(B)** FI values obtained from fluorescence staining.

References

1. Baier Leach, J., et al., *Photocrosslinked hyaluronic acid hydrogels: Natural, biodegradable tissue engineering scaffolds.* Biotechnology and Bioengineering, 2003. **82**(5): p. 578-589.

2. Richbourg, N.R., et al., Precise control of synthetic hydrogel network structure via linear, independent synthesis-swelling relationships. Science Advances, 2021. **7**(7): p. eabe3245.